Uncertainties identification of [..[*]]blade-mounted lidar-based inflow wind speed measurements for robust feedback-feedforward control synthesis

Róbert Ungurán[1], Vlaho Petrović[1], Lucy Y. Pao[2], and Martin Kühn[1]

[1]ForWind, University of Oldenburg, Institute of Physics, Küpkersweg 70, 26129 Oldenburg, Germany
[2]Department of Electrical, Computer, and Energy Engineering, University of Colorado, Boulder, USA

Correspondence to: Róbert Ungurán (robert.unguran@uni-oldenburg.de)

Abstract. The current trend toward larger wind turbine rotors leads to high periodic loads across the components due to the non-uniformity of inflow across the rotor. [..[2]]To address this, we introduce a blade-mounted lidar on each blade to provide a preview of inflow wind speed that can be used as a feedforward control input for the mitigation of such periodic blade loads. We present a method to easily determine blade-mounted lidar parameters, such as focus distance, telescope position, and orientation on the blade. However, such a method is accompanied by uncertainties in the inflow wind speed measurement, which may also be due to the induction zone, wind evolution, "cyclops dilemma", unidentified misalignment in the telescope orientation, and the blade segment orientation sensor. Identification of these uncertainties allows their inclusion in the feedback–feedforward controller development for load mitigation. We perform large-eddy simulations, in which we simulate the blade-mounted lidar including the dynamic behaviour and the induction zone of one reference wind turbine for one [..[3]]above-rated inflow wind speed. Our calculation approach provides a good trade-off between a fast-and-simple determination of the telescope parameters and an accurate inflow wind speed measurement. We identify and model the uncertainties, which then can directly be included in the feedback-feedforward controller design and analysis. The rotor induction effect increases the preview time, which needs to be considered in the controller development and implementation.

1 Introduction

The ongoing trend of steadily growing rotor [..[4]]diameters of wind turbines results in dynamic loads across the rotor swept area, which are becoming more uneven. Due to the so-called rotational sampling or eddy slicing effect, the blade samples the inhomogeneous wind field with frequencies determined by the rotor speed. Hence, the dynamic blade loads [..[5]]are concentrated at the multiples of the rotational frequency, i.e., 1P, 2P, 3P,...,nP (Bossanyi (2003); van Engelen (2006)).

[*]removed: the

[2]removed: On thisregard

[3]removed: above rated

[4]removed: diameter

[5]removed: gets

The scope of this paper is particularly geared to the relevance of three aspects of recent developments in controls to mitigate such loading. First, the control surfaces on the rotor are becoming more localized and consequently [..[6]]in addition to individual (blade) pitch control, local active or passive blade load mitigation concepts (e.g. trailing edge flaps) have been researched for several years. Second, in addition to the proven feedback control triggered by rotor speed or the individual blade root bending moments, feedforward control using either observer techniques or lidar-assisted preview information of the inflow is investigated for collective or individual pitch as well as trailing edge flap control. Third, special attention is required in the feedback–feedforward controller design to guarantee robust stability and performance in the presence of inherent uncertainties in the lidar measurement.

The traditional collective pitch control (CPC) is responsible for keeping the rotor speed constant near and [..[7]]at above-rated wind speed conditions. Bossanyi (2003) extended the CPC with individual pitch control (IPC) to mitigate the 1P dynamic blade load. The effectiveness of the IPC in reducing the dynamic blade loads is demonstrated in this paper. Later, the function of the IPC was extended to address the mitigation of higher harmonic dynamic blade loads (Bossanyi (2005); van Engelen (2006)), leading to load relief across the wind turbine components, i.e., blade root bending moments, hub yaw and tilt moments, yaw bearings, etc. Such a control design leads to the increased use of the blade pitch system. With growing blade length, the blade mass rises with a power of two to three, and thus, increased pitch activity becomes even more undesirable, and as such results in wear and tear of the pitch actuators and bearings and equivalently, higher maintenance costs. One solution involves the use of small localized control surfaces to locally influence the thrust force, e.g., close to the blade tip, which contributes greatly to the overall blade root loadings. Pechlivanoglou (2013) conducted experimental and numerical studies to determine the most promising setup of passive and active local flow control solutions for wind turbine blades, and he concluded that a controllable flexible trailing edge flap close to the blade tip has the most potential to mitigate the dynamic blade loads. The individual trailing edge flap control (TEFC) [..[8]]has been shown to be an effective means of reducing dynamic blade loads [..[9]]in numerical studies (Bergami and Poulsen (2015); He et al. (2018); Ungurán and Kühn (2016); Zhang et al. (2018)), wind tunnel tests (Barlas et al. (2013); Marten et al. (2018); van Wingerden et al. (2011)), and field tests (Berg et al. (2014); Castaignet et al. (2014)). Castaignet et al. (2014) performed a full-scale test on [..[10]]a Vestas V27 wind turbine, reporting a load reduction of 14% at the flap-wise blade root bending moment, providing proof of the control concept and the capabilities of the trailing edge flap for dynamic blade loads mitigation.

Recently, feedforward control has been identified as a promising concept for wind turbine control, as [..[11]]feedback controller mainly rely on indirect measurement of the disturbance, e.g., through measurement of rotor speed deviation from rated rotor speed or measurement of the blade root bending moment. Feedback controllers are only able to react on the disturbance after its influence on the wind turbine has been measured, which leads to a delayed control action. Several authors propose lidar-assisted wind turbine controllers so that control actions can be determined before the disturbance influences the turbine.

[6]removed: beside
[7]removed: above rated
[8]removed: is proven as
[9]removed: reductions
[10]removed: the
[11]removed: it mainly relies

When properly tuned, this so-called feedforward control strategy can mitigate fatigue loading from external disturbances. The lidar-assisted collective pitch controller proposed by Schlipf et al. (2013) accomplished a better rotor speed tracking with reduced pitch activity, with respect to the feedback collective pitch controller. They demonstrated the reduction of damage equivalent loads at the out-of-plane blade root bending moment, low-speed shaft torque, and tower bottom fore-aft bending moment through the use of lidar as feedforward collective pitch control input. Bossanyi et al. (2014); Kapp (2017) investigated the use of lidar for feedback–feedforward collective and individual pitch control and concluded its suitability for wind turbine control applications. Their purpose for the IPC was to mitigate the 1P loads at the flapwise blade root bending moment. They observed that a lidar-assisted feedback–feedforward IPC achieves marginal damage equivalent loads reduction with respect to feedback-only IPC. Ungurán et al. (2019) achieved additional load reduction across various wind turbine components with [..[12]]a combined feedback–feedforward IPC [..[13]]when compared to feedback-only IPC. They highlighted that to further reduce the blade root bending moment and avoid undesirable load [..[14]]increases on other wind turbine components, special care should be taken as the feedback is combined with feedforward IPC during controller development, in terms of, for instance, avoiding the same bandwidth for the feedback and feedforward IPC. This results in an elevated peak in the sensitivity function around the crossover frequency. Furthermore, Bossanyi et al. (2014); Kapp (2017); Ungurán et al. (2019) studied different inflow wind conditions and wind turbine characteristics; they, also used different lidar systems for feedforward control purposes that influenced the results.

Due to obvious reasons, it is necessary to consider the uncertainties in the lidar measurements to achieve robust stability and performance of the feedback–feedforward controller. Furthermore, the source of such uncertainties must be identified and modeled, which can then be incorporated into the design and analysis of the controller, to ensure performance even for uncertain lidar measurements. Several authors have already addressed this problem, e.g., Bossanyi (2013); Laks et al. (2013); Simley et al. (2014a, b) with their numerical investigations. Simley et al. (2016) performed field tests to assess the influence of the "cyclops dilemma", spatial averaging error, induction zone, and wind evolution, on a hub-mounted lidar measurement. Simley et al. (2014a) used a hub-mounted continuous-wave (CW) lidar to investigate the effect of the "cyclops dilemma," and concluded the existence of a compromise in the preview distance. Spatial averaging increases with increasing distance from the rotor plane, leading to correlation attenuation between the rotor-effective wind speed and the lidar-estimated inflow wind speed, with increasing frequency. As [..[15]]measurements are taken closer to the rotor plane, the contribution of the lateral and vertical wind components to the line-of-sight lidar measurements also increases. [..[16]]Thus, it is not possible to accurately reconstruct the longitudinal wind component from a single hub-mounted lidar system, which results in over- or underestimation of the rotor effective wind speed. Laks et al. (2013) investigated how wind evolution affects controller performance; they used a single point measurement, without spatial averaging, in front of the wind turbine blade as a feedforward IPC input. Using the feedback–feedforward IPC, they acquired the highest load reduction at the blade root bending moment at a preview time of

[12]removed: the

[13]removed: with respect

[14]removed: increase

[15]removed: measurement gets

[16]removed: Nevertheless

only 0.2 s. The further the measurement was taken from the rotor plane, the more the wind evolved on high frequencies (i.e., the so-called "wind evolution"), leading to overactuation by the feedforward IPC. It should be noted that the required preview time depends on many factors, e.g., wind turbine size, 1P frequency, inflow wind speed, induced phase shift by the feedforward controller and blade pitch actuators, etc.

The blade-mounted lidar system is a novel technique that enables us to sample the wind component parallel to the rotor shaft axis around the swept area (Bossanyi (2013)) and has [..[17]]been demonstrated to be technologically viable (Mikkelsen et al. (2012)). Such a feature of the system enables addressing the mitigation of higher harmonic dynamic blade loads through feedback–feedforward individual pitch and trailing edge flap controllers (Ungurán et al. (2018, 2019)), while simultaneously posing challenges with the presence of the induction zone. The closer the lidar measurement is taken to the rotor plane, the higher the deficit between the measured inflow and free flow wind speeds. Additionally, this deficit depends on where the lidar is mounted along the blade radius, which shows the importance of [..[18]]analysing how the blade-mounted lidar measurement is affected by [..[19]]wind evolution, the induction zone, and the assumptions made during the inflow wind speed reconstruction.

Therefore, in this study, our objective is to identify the nominal measurement transfer functions and model the uncertainties of the blade-mounted lidar measurement as a frequency-dependent uncertain weight for inclusion into the feedback–feedforward individual pitch and trailing edge flap control development, and to [..[20]]analyse the impact of the induction zone effect on the preview time.

The rest of the paper is organized as follows: Section 2 provides a description of the framework and methods we [..[21]]use for identifying the uncertainties and preview time of the blade-mounted lidar measurement, [..[22]]after an introduction of the blade-mounted lidar-based simulation setup in Section 2.1. In Section 2.2 we describe the method we use to estimate the inflow wind speed. The method we employed for determining the blade effective wind speed to assess the efficiency of the blade-mounted lidar-based inflow wind speed measurement is discussed in Section 2.3. Section 2.4 describes the general control implementation and presents the multiblade coordinate transformation and its importance in the controller design, while Section 2.5 details how the lidar-based measurement uncertainty in considered in control development and analysis. Section 2.6 proposes a method to identify the uncertainties of the blade-mounted lidar measurement as a frequency-dependent uncertainty weight, [..[23]]Section 2.7 presents the method [..[24]]we apply for estimating the preview time[..[25]], and Section 2.1 introduces a const function which we use to evaluate the initially selected lidar and telescope parameters. The results of a reference case are presented in Section 3, [..[26]]where in Section 3.1 we analyse the effect of the multiblade coordinate transformation

[17]removed: be
[18]removed: analyzing
[19]removed: the
[20]removed: analyze
[21]removed: used
[22]removed: followed by
[23]removed: whereas
[24]removed: for
[25]removed: estimation.
[26]removed: with the establishment of the simulation setup (Section 3.2), an analysis on

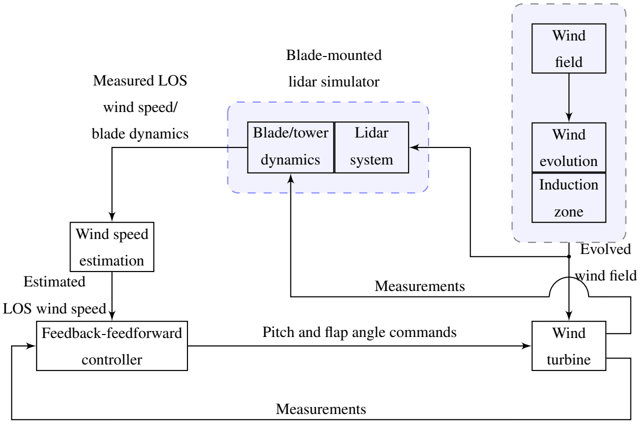

Figure 1. Block diagram of the blade-mounted lidar-based simulation setup. LOS corresponds to line-of-sight.

[..[27]]on the measurement. The simulation setup is established in Section 3.2, and we systematic analyse the uncertainties of various telescope and control parameters [..[28]]in Section 3.3. The results are discussed in Section 4 prior to the conclusions in Section 5.

2 Methodology

2.1 Blade-mounted lidar

A telescope [..[29]]is mounted on each blade and [..[30]]is connected to a hub-based continuous-wave lidar with [..[31]]fibre optical cables. The lidar [..[32]]samples the inflow wind speed in front of the rotor plane at a rate of 5 Hz, [..[33]]and we intend to use the lidar measurements for control purposes. The lidar [..[34]]measurements are integrated into the system model according to Figure 1, [..[35]]and we use a combination of large-eddy simulations and an aeroelastic simulation code [..[36]]to simulate and evaluate the lidar-based inflow measurements. Thus, lidar measurements are simulated in a realistic environment, where the effect of the induction zone and wind evolution, as well as the dynamic behaviour of the wind turbine, [..[37]]are taken into account. Moreover, the lidar simulator [..[38]]considers volumetric measurement, dynamics of the blade and tower,

[27] removed: (Section 3.1), and a systematic analysis of
[28] removed: (Section 3.3). Results of this paper
[29] removed: was
[30] removed: was
[31] removed: fiber
[32] removed: sampled
[33] removed: which
[34] removed: measurement was
[35] removed: through
[36] removed: . This enabled to simulate the lidar measurement
[37] removed: were
[38] removed: considered

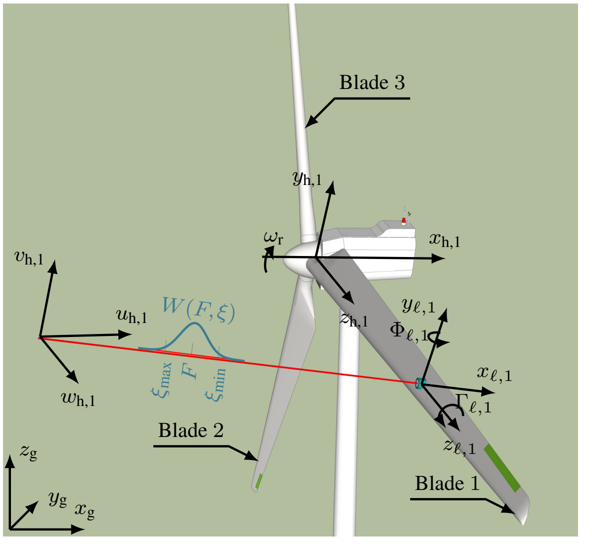

Figure 2. Configuration of the lidar measurement system, with a telescope mounted on each blade and connected to a continuous-wave lidar in the hub via [..[40]]fibre optics. The line-of-sight wind speed is computed on the basis of a weighting function ($W(F,\xi)$), which is dependent on the focus distance (F) and the range along the beam (ξ).

i.e., displacement, rotation, and linear velocity in 3D space, and blade-rotation-induced velocity. Nevertheless, the rotational effect of the blade [..[39]]is not accounted for during the accumulation of a single measurement.

Figure 2 illustrates the coordinate systems and the telescope orientation. Here, the line-of-sight (LOS) wind speed measurement from blade i ($u_{\mathrm{los},i}$) [..[41]]is defined as

$$u_{\mathrm{los},i} = \frac{\int_{\xi_{\mathrm{min}}}^{\xi_{\mathrm{max}}} W(F,\xi)\, V_i(\xi)\, d\xi}{\int_{\xi_{\mathrm{min}}}^{\xi_{\mathrm{max}}} W(F,\xi)\, d\xi}\,, \tag{1}$$

where $V_i(\xi)$ is defined in Equation (3), $W(F,\xi)$ is the lidar's weighting function, defined according to Simley et al. (2014a) as

$$W(F,\xi) = \frac{1}{\xi^2 + \left(1 - \frac{\xi}{F}\right)^2 R_{\mathrm{R}}^2}\,, \tag{2}$$

where R_{R} is the Rayleigh range, set at 1,573 m herein, as proposed by Simley et al. (2014a); F is the focus distance and ξ is the range along the beam. Limits ξ_{min} and ξ_{max}, introduced in Equation (1), refer to the minimum and maximum range,

[39] removed: was
[41] removed: could be

respectively, along the beam. For practical implementation of the lidar simulator, these values [..[42]]are chosen such that $\frac{W(F,\xi)}{W(F,F)}$ equals 0.02 at these limits. During discretization of Equation (1), the spatial resolution [..[43]]is set empirically at $\Delta\xi = 0.1$ m. A single-point measurement is given by

$$V_i(\xi) \quad = \quad \left(\begin{bmatrix} u_{\mathrm{h},i}(\xi) \\ v_{\mathrm{h},i}(\xi) \\ w_{\mathrm{h},i}(\xi) \end{bmatrix} - \begin{bmatrix} \dot{x}_{\mathrm{t,h},i} \\ \dot{y}_{\mathrm{t,h},i} \\ \dot{z}_{\mathrm{t,h},i} \end{bmatrix} \right)^T \begin{bmatrix} \ell_{\mathrm{x,h},i} \\ \ell_{\mathrm{y,h},i} \\ \ell_{\mathrm{z,h},i} \end{bmatrix} , \tag{3}$$

where $[u_{\mathrm{h},i}\ v_{\mathrm{h},i}\ w_{\mathrm{h},i}]^T$ is the wind speed vector along the laser beam expressed in the rotating hub coordinate system; $[\dot{x}_{\mathrm{t,h},i}\ \dot{y}_{\mathrm{t,h},i}\ \dot{z}_{\mathrm{t,h},i}]^T$ is the linear velocity vector of the blade segment where the telescope is mounted, expressed in the rotating hub frame of reference[..[44]]; and $[\ell_{\mathrm{x,h},i}\ \ell_{\mathrm{y,h},i}\ \ell_{\mathrm{z,h},i}]^T$ is the unit vector of the laser beam in the rotating hub coordinate system. The aeroelastic simulation tool is capable of providing full kinematics information, i.e., positions, orientations, and linear and angular velocities, of any blade segment in the hub coordinate system.

2.2 Wind speed estimation

During the inflow wind speed estimation, the velocity, displacement, and rotation of the blade segment [..[45]]are assumed to be known; therefore, the [..[46]]wind speed component parallel with the rotor shaft axis can be reconstructed as indicated in Equation (4).

Without loss of generality, [..[47]]in the wind speed estimation, the weighting function of $W(F,\xi)$ from Equation (1) is neglected, and two assumptions are made: (1) the $v_{\mathrm{h},i}$ and $w_{\mathrm{h},i}$ components are zero and (2) the mean wind [..[48]]velocity is parallel with the rotor axis, i.e., no tilt and no yaw [..[49]]misalignments are considered. Consequently, an estimate of the wind speed parallel to the rotor shaft axis ($u_{\mathrm{h,est},i}$) [..[50]]is

$$u_{\mathrm{h,est},i} \quad \approx \quad \frac{u_{\mathrm{los},i} + \dot{y}_{\mathrm{t,h},i}\ell_{\mathrm{y,h},i} + \dot{z}_{\mathrm{t,h},i}\ell_{\mathrm{z,h},i}}{\ell_{\mathrm{x,h},i}} + \dot{x}_{\mathrm{t,h},i} \quad . \tag{4}$$

Nevertheless, such assumptions [..[51]]introduce errors in the lidar measurement that [..[52]]are presumed to exist in the identified uncertainty weight, and thus, [..[53]]are consequently considered during the controller development.

[42] removed: were
[43] removed: was
[44] removed: and;
[45] removed: were
[46] removed: measured LOS wind speed can be corrected
[47] removed: two assumptions were
[48] removed: speed
[49] removed: misalignment is
[50] removed: can be estimated as
[51] removed: introduced
[52] removed: were
[53] removed: were

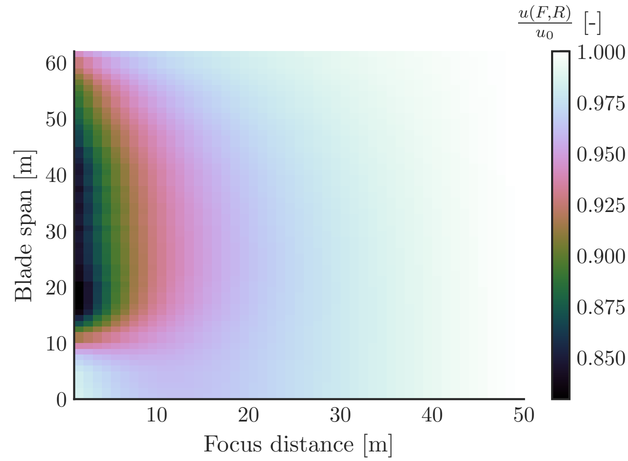

Figure 3. Normalized longitudinal inflow wind speed ($\frac{u(F,R)}{u_0}$) [..[58]]as a function of focus distance (F) and blade span position (R), with an undisturbed inflow wind speed $u_0 = 13\,\mathrm{m\,s^{-1}}$.

2.3 [..[54]]

[..[55]]

[..[56]]

[..[57]]

Figure 3 illustrates the induction zone effect for the reference case defined in [..[59]]Section 3.3. Note that the lidar measurement [..[60]]is affected by the rotor induction. The reduction depends on the position of the telescope along the blade radius (R) and the focus distance of the laser beam (F), where the wind speed measurement takes place. To account for this effect in the lidar-based inflow wind speed measurement, we [..[61]]construct a second-order polynomial function (f), whose inputs [..[62]]are chosen as rotor speed (ω_r), blade pitch angle (β_i), and blade root flapwise and edgewise moments ($M_{\mathrm{fw},i}$, $M_{\mathrm{ew},i}$). Rotor speed and blade pitch angles are easily measured, and we assumed that the blade root flapwise and edgewise moment sensors are also available for implementing this method. Therefore, the estimated wind speed parallel to the rotor shaft axis

[54] removed: Blade effective wind speed and wind speed deficit estimation

[55] removed: To assess the performance efficiency of the blade-mounted lidar-based inflow wind speed measurement, we introduced a new signal called the blade-effective wind speed ($u_{\mathrm{beff},i}$), which is determined as the contribution of the inflow wind speed on each blade segment $u_i(r)$ to the flapwise blade root bending moment; the inflow wind speed refers to the longitudinal wind speed in the rotor axis direction. The contribution depends on the radial distance (r) and the local thrust coefficient (C_T) of the blade segment as expressed by

[57] removed: The local thrust coefficients were resolved from steady-state simulations for each blade segment from cut-in to cut-out wind speeds.

[59] removed: Section 3.2

[60] removed: was

[61] removed: constructed

[62] removed: were chosen from widely available wind turbine sensors, such

($u_{\text{h,est},i}$) is corrected as

$$u_{\text{cor},i} \quad = \quad u_{\text{h,est},i} + \Delta u_{\text{est},i} \quad , \tag{5}$$

where

$$u_0 - u(F,R) \approx \Delta u_{\text{est},i} = f(F,R,\omega_{\text{r}},\beta_i,M_{\text{fw},i},M_{\text{ew},i}) \quad . \tag{6}$$

The second-order polynomial function (f) is fitted on the data extracted from 10-minute large-eddy simulations with laminar inflow for mean wind speeds between $4\,\text{m}\,\text{s}^{-1}$ and $25\,\text{m}\,\text{s}^{-1}$. The $u(F,R)$ is the wind speed at an upstream distance from the blade of F, and at a blade radial position of R, and u_0 is taken from the same blade radial position of R, but at an upstream distance of three times the rotor diameter (3D).

2.3 Blade effective wind speed

To assess the performance efficiency of the blade-mounted lidar-based inflow wind speed measurement, we introduce a new signal called the blade-effective wind speed ($u_{\text{beff},i}$), which is determined as the contribution of the inflow wind speed on each blade segment $u_i(r)$ to the flapwise blade root bending moment; the inflow wind speed refers to the longitudinal wind speed in the rotor axis direction. The contribution depends on the radial distance (r) and the local thrust coefficient (C_{T}) of the blade segment as expressed by

$$u_{\text{beff},i} \quad = \quad \sqrt{\frac{\int_{R_{\text{hub}}}^{R_{\text{tip}}} C_{\text{T}}(r,u_i(r))\, r^2\, u_i^2(r)\, dr}{\int_{R_{\text{hub}}}^{R_{\text{tip}}} C_{\text{T}}(r,u_i(r))\, r^2\, dr}} \quad . \tag{7}$$

The local thrust coefficients are resolved from steady-state simulations for each blade segment from cut-in to cut-out wind speeds.

2.4 Multiblade coordinate transformation (MBC)

In the subsequent step, we [..[63]]introduce the multiblade coordinate transformation (MBC) that simplifies the controller design by transforming a time-varying system into a time-invariant system and decouples the individual pitch from the collective pitch control. Figure 4 demonstrates the manner in which the feedforward controller [..[68]]is implemented. First, the measured inflow wind speed [..[69]]is transformed to the non-rotating frame of reference by applying MBC transformation ($T_{\text{mbc}}(\theta+\phi)$)

[63] removed: introduced
[68] removed: was
[69] removed: was

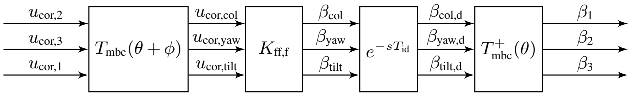

Figure 4. Implementation of the feedforward collective and individual pitch control, where the inputs ($u_{\mathrm{cor},1}$, $u_{\mathrm{cor},2}$, and $u_{\mathrm{cor},3}$) are the estimated wind speeds parallel to the rotor shaft axis and the outputs are the blade pitch angles (β_1, β_2, and β_3). The feedforward controller ($K_{\mathrm{ff,f}}$) [..[64]]is implemented in the non-rotating (fixed) frame of the reference and [..[65]]is, therefore, denoted with an extra index f. Further, the multi-blade coordinate transformation (T_{mbc}) [..[66]]is applied to the inputs, and the pseudo-inverse transformation (T^{+}_{mbc}) [..[67]]is applied to the outputs.

in accordance with Equation (8), where θ denotes the azimuth angle.

$$\begin{bmatrix} u_{\mathrm{cor,col}} \\ u_{\mathrm{cor,yaw}} \\ u_{\mathrm{cor,tilt}} \end{bmatrix} = T_{\mathrm{mbc}}(\theta+\phi) \begin{bmatrix} u_{\mathrm{cor},2} \\ u_{\mathrm{cor},3} \\ u_{\mathrm{cor},1} \end{bmatrix} \tag{8}$$

where

$$T_{\mathrm{mbc}}(\theta) = \begin{bmatrix} \frac{1}{3} & \frac{1}{3} & \frac{1}{3} \\ \frac{2}{3}\cos(n_{\mathrm{h}}\theta) & \frac{2}{3}\cos\left(n_{\mathrm{h}}\left[\theta+\frac{2\pi}{3}\right]\right) & \frac{2}{3}\cos\left(n_{\mathrm{h}}\left[\theta+\frac{4\pi}{3}\right]\right) \\ \frac{2}{3}\sin(n_{\mathrm{h}}\theta) & \frac{2}{3}\sin\left(n_{\mathrm{h}}\left[\theta+\frac{2\pi}{3}\right]\right) & \frac{2}{3}\sin\left(n_{\mathrm{h}}\left[\theta+\frac{4\pi}{3}\right]\right) \end{bmatrix}. \tag{9}$$

A phase shift (ϕ) [..[70]]is introduced into the transformation to consider that the measured inflow wind speed hits the wind turbine blade after this azimuth angle change. This value varies with respect to several parameters, including the selected focus distance, inflow wind speed, and rotor speed. Further, the control signals or the blade pitch angles (β_{col}, β_{yaw}, β_{tilt}) [..[71]]are determined by the feedforward controller ($K_{\mathrm{ff,f}}$). If the preview time provided by the lidar [..[72]]is greater than the time delay induced by the feedforward controller, an additional time delay ($e^{-sT_{\mathrm{id}}}$) [..[73]]is introduced into the system. Finally, the delayed control signals ($\beta_{\mathrm{col,d}}$, $\beta_{\mathrm{yaw,d}}$, and $\beta_{\mathrm{tilt,d}}$) [..[74]]are transformed to the rotating frame of the reference using the pseudo-inverse of the MBC transformation ($T^{+}_{\mathrm{mbc}}(\theta)$). The main structure of the feedforward individual pitch controller in Figure 4 can be used in the feedforward trailing edge flap controller as well.

The MBC transformation plays a considerably important role because it can transform a frequency component of interest, such as 1P, 2P, or 3P (Bossanyi (2003); van Engelen (2006)), to a low-frequency component, named as 0P. It is dependent on the selected value of n_{h} in [..[75]]Equation (9). For example, 1P will be transformed to 0P when n_{h} is specified as 1, and 2P will be transformed to 0P when n_{h} is specified as 2.

[70]removed: was
[71]removed: were
[72]removed: was higher
[73]removed: was
[74]removed: were
[75]removed: Equation (8)

In this study, we focus on identifying the uncertainty weight that can be used during the feedback-feedforward individual and collective pitch control development with an objective to mitigate the 1P loads at the flapwise blade root bending moments and to enhance the rotor speed tracking. This indicates that the measured inflow wind speeds [..[76]]are transformed to the non-rotating frame of reference by considering n_{h} as 1 in [..[77]]Equation (9), where the uncertainty weight identification [..[78]]is conducted. Further, the same methodology can be applied to identify the uncertainty weight for high harmonics control by selecting a large integer value of n_{h}.

We have already mentioned that the measured inflow wind speeds were transformed to the non-rotating frame of reference by applying the MBC transformation. In order to assess the performance efficiency of the blade-mounted lidar-based inflow wind speed measurement, the blade effective wind speeds were also transferred into the non-rotating frame using the MBC transformation as follows

$$\begin{bmatrix} u_{\mathrm{bef,col}} \\ u_{\mathrm{bef,yaw}} \\ u_{\mathrm{bef,tilt}} \end{bmatrix} = \mathsf{T}_{\mathrm{mbc}}(\theta) \begin{bmatrix} u_{\mathrm{bef,1}} \\ u_{\mathrm{bef,2}} \\ u_{\mathrm{bef,3}} \end{bmatrix} \tag{10}$$

where $T_{\mathrm{mbc}}(\theta)$ is defined in Equation (9).

2.5 System modeling with uncertain lidar measurements

We [..[79]]use the blade-mounted telescopes to measure the disturbance, or the inflow wind speed in this case. Afterward, the three measurements [..[80]]are transformed into the non-rotating frame of reference where they [..[81]]are used as inputs to the feedforward individual and collective pitch controllers. Figure 5 illustrates the disturbance rejection controller setup with uncertainty. Each block in the figure represents a three-input and three-output system. Consequently, the resulting transfer function [..[82]]is in a 3×3 matrix (three-input and three-output). The measurement uncertainty can vary with wind speed, wind shear, turbulence intensity, etc. (Navalkar et al. (2015)), thus, multiplicative diagonal complex uncertainties [..[83]]are considered.

The control development [..[84]]is aimed at achieving disturbance rejection up to a certain frequency with measurement uncertainties. In other words, we [..[85]]want to find a controller that satisfies Equation (11) for a chosen performance weight W_{p}.

$$\left\| W_{\mathrm{p}} S_{\mathrm{fb}} S_{\mathrm{ff,p}} \right\|_{\infty} < 1, \tag{11}$$

[76] removed: were
[77] removed: Equation (8)
[78] removed: was
[79] removed: used
[80] removed: were
[81] removed: were
[82] removed: was
[83] removed: were considered.
[84] removed: was
[85] removed: wanted

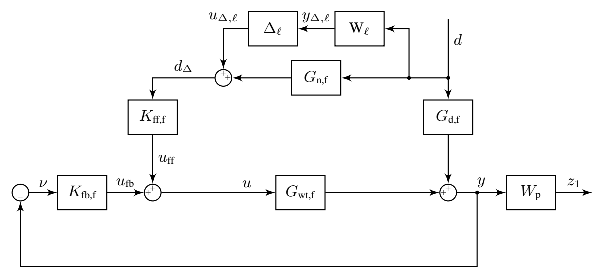

Figure 5. Block diagram of the disturbance rejection control design with performance weight and uncertain input measurement. $K_{\mathrm{fb,f}}$, $K_{\mathrm{ff,f}}$ are the feedback and feedforward controllers, $G_{\mathrm{wt,f}}$ is the wind turbine model from the control input to output, $G_{\mathrm{d,f}}$ is the wind turbine model from the disturbance to the output, $G_{\mathrm{n,f}}$ is the nominal disturbance measurement model, Δ_ℓ is the uncertainty, W_ℓ is the measurement uncertainty weight, and W_{p} is the performance weight. The f in the index refers to the non-rotating (fixed) frame of reference.

where the frequency-dependent feedback (S_{fb}) and feedforward sensitivity ($S_{\mathrm{ff,p}}$) functions with [..[86]]additive uncertainty are given by

$$
\begin{aligned}
S_{\mathrm{fb}} &= \left(I + G_{\mathrm{wt,f}} K_{\mathrm{fb,f}}\right)^{-1} \\
S_{\mathrm{ff,p}} &= I + G_{\mathrm{wt,f}} K_{\mathrm{ff,f}} \left(G_{\mathrm{n,f}} + \Delta_\ell W_\ell\right) G_{\mathrm{d,f}}^{-1}
\end{aligned}
\tag{12}
$$

and

$$
\Delta_\ell = \begin{bmatrix} \delta_{\ell,1} & 0 & 0 \\ 0 & \delta_{\ell,2} & 0 \\ 0 & 0 & \delta_{\ell,3} \end{bmatrix} \in \mathbb{C}^{3\times 3} \quad [..[87]]
\tag{13}
$$

[..[88]]and satisfies the property $||\Delta_\ell||_\infty \leq 1$. This equation highlights the importance of knowing the frequency-dependent uncertainty weight $W_\ell(j\omega)$ in advance, so as to ensure that the closed-loop system is stable and that the objective in Equation (11) is satisfied for all perturbations ($||\Delta_\ell||_\infty \leq 1$). For control development, only the identification of the frequency dependent uncertainty weight of $W_\ell(j\omega)$ [..[89]]and the nominal disturbance measurement model of $G_{\mathrm{n,f}}(j\omega)$ are missing, which [..[90]]are identified for the reference [..[91]]cases in Section 3.3.

[..[92]]Remark: [..[93]]Only one objective [..[94]]is introduced in Equation (11); nevertheless, other objectives can be added, such as penalizing the control signal magnitude at high frequencies (Ungurán et al. (2019)). [..[95]]

[..[96]]

[86]removed: multiplicative
[88]removed: for
[89]removed: was
[90]removed: was
[91]removed: case
[92]removed: Remarks
[93]removed: (1)
[94]removed: was
[95]removed: (2) To avoid the disturbance model acting as a scaling factor of the objective function, as in

[..[97]]

[..[98]]

[..[99]]

2.6 Uncertainty modeling for control development

We [..[100]]employ black box system identification to establish the transfer functions (G_ℓ) from the blade effective wind speeds (u_{beff}) to the corrected [..[101]]lidar-based inflow wind speeds (u_{cor}) in the non-rotating (fixed) frame of reference

$$u_{\text{cor,f}} \quad = \quad G_\ell \, u_{\text{beff,f}} \tag{14}$$

with

$$G_\ell \quad = \quad \begin{bmatrix} G_{\ell,\text{col}} & 0 & 0 \\ 0 & G_{\ell,\text{yaw}} & 0 \\ 0 & 0 & G_{\ell,\text{tilt}} \end{bmatrix} \in \mathbb{C}^{3\times 3} \quad . \tag{15}$$

The system identification is performed via the `ssest` function from MATLAB (2018) with a 15th-order state-space model, which can capture all the relevant information. The order of the state-space model [..[102]]is found empirically.

We separately [..[103]]identify the nominal disturbance measurement model ($G_{\text{n},k}(j\,\omega)$) and the [..[104]]

[..[105]]

[..[106]]

[..[107]]

uncertainty weight ($w_{\ell,k}(j\,\omega)$), where

[..[108]]

[..[109]]$k \in \{\text{col, yaw, tilt}\}$, as a 5th-order minimum phase filter for each of the inputs in such a way as to satisfy the following inequalities

$$|G_{\text{n},k}(j\,\omega)| \quad < \quad |G_{\ell,k}(j\,\omega)|, \; \forall \omega, \tag{16}$$

[97]removed: Figure 5 was extended with the inverse of the disturbance model ($G_{\text{d,f}}^{-1}$) (shown in a dashed rectangle), so that

[99]removed: which ensures that z_1 is not affected by the disturbance model. Hence, in the control synthesis and analysis, z_1 is a direct indicator of the controller performance in the presence of uncertainties.

[100]removed: employed

[101]removed: lidar based

[102]removed: was

[103]removed: identified the uncertainty weight for each of the inputs ($w_{\ell,k}(j\,\omega)$) in such a way as to ensure that the relative error between the nominal

[104]removed: identified systems ($G_{\ell,k}(j\,\omega)$) is below each uncertainty weight

[106]removed: The uncertainty weight is modeled as a first-order minimum-phase filter

[109]removed: Here, $w_{\text{DC},k} = w_{\ell,k}(j\,0)$ and $w_{\infty,k} = w_{\ell,k}(j\,\infty)$ represent the DC and high-frequency gains of the filter, and correspond to the uncertainties at low and high frequencies, respectively. The crossover frequency $\omega_{0,k}$ is defined as the frequency where the magnitude of the filter crosses 1 from below ($|w_{\ell,k}(j\,\omega_{0,k})| = 1$), or 0 dB, and with

and

$$|G_{\mathrm{n},k}(j\omega)+w_{\ell,k}(j\omega)| \quad > \quad |G_{\ell,k}(j\omega)|,\ \forall\omega, \tag{17}$$

leading to the [..[110]]diagonal nominal disturbance measurement model matrix of

$$G_{\mathrm{n}} = \begin{bmatrix} G_{\mathrm{n,col}} & 0 & 0 \\ 0 & G_{\mathrm{n,yaw}} & 0 \\ 0 & 0 & G_{\mathrm{n,tilt}} \end{bmatrix}, \tag{18}$$

[..[111]]and [..[112]]uncertainty weight matrix of

$$W_{\ell} = \begin{bmatrix} w_{\ell,\mathrm{col}} & 0 & 0 \\ 0 & w_{\ell,\mathrm{yaw}} & 0 \\ 0 & 0 & w_{\ell,\mathrm{tilt}} \end{bmatrix}. \tag{19}$$

The order of the transfer functions are determined empirically during the analysis of the data. Lower orders could be selected as well, however, these would lead to higher uncertainties at high frequency.

The ideal case would be to measure with a telescope, the exact inflow wind speed hitting the rotor blades, to result in a nominal disturbance measurement transfer function with a gain of 1 over the entire frequency range. [..[113]]However, not only the inflow condition, but also the telescope parameters are influencing the nominal disturbance measurement model and the measurement uncertainty weight. In Section 3.3 we identify these transfer functions ($G_{\mathrm{n},k}$ [..[114]]and $w_{\ell,k}$) which then can be used for control development and analysis. Furthermore, we analyse how much the low-frequency gains of G_ℓ deviate from 1 for several cases.

We neglect the cross-coupling between the yaw and tilt components in the system identification, but these [..[115]]are considered in the wind turbine and disturbance transfer functions in line with Lu et al. (2015), so that the cross-coupling between the yaw and tilt components is included in the controller development.

2.7 Preview time estimation

Preview time plays an important role in the development of feedforward control. It must be larger than or equal to the time delay introduced by the feedforward controller and actuator dynamics. It is preferable to be equal, but a larger value is acceptable, as additional time delay can be easily introduced into the feedforward controller, as shown in Figure 4. To determine the optimal preview time for a given focus distance, we [..[116]]evaluate the cross-correlation between the blade effective ($u_{\mathrm{beff},k}$) and the

[110] removed: frequency-dependent diagonal weighting matrix of

[111] removed: which can be used in the feedback–feedforward IPC control development and analysis. The expressions $w_{\mathrm{DC},k}$, $w_{\infty,k}$,

[112] removed: $\omega_{0,k}$ are identified for several cases in Section 3.3

[113] removed: Therefore, we chose a first-order Butterworth low-pass filter with a cut-off frequency of 10 Hz and a gain of 1, as the nominal system

[114] removed:). With the lidar having a sampling rate of 5 Hz, we ensured that the gain up to 2.5 Hz was close to 1. Higher frequencies were not studied in this work. We neglected

[115] removed: were

[116] removed: built three functions (J_k) based on the coherence (γ_k^2) and phase shift (φ_k)

corrected inflow ($u_{\mathrm{cor},k}$) wind speeds, with $k \in \{\mathrm{col, yaw, tilt}\}$[..[117]]

[..[118]]

[..[119]], and we choose the index of the peak value as the available preview time.

3 [..[120]]

2.1 [..[121]]Telescope parameters estimation

[..[122]][..[123]][..[124]]

[..[125]]We introduce a cost function which is based only on the coherence (γ_k^2) between the blade effective ($u_{\mathrm{beff},k}$) and the corrected inflow ($u_{\mathrm{cor},k}$) wind speeds, with $k \in \{\mathrm{col, yaw, tilt}\}$:

$$J_{\mathrm{lp}} = \sum_k J_{\mathrm{lp},k} = \sum_k \gamma_k^2(f) \ . \tag{20}$$

By evaluating J_{lp} for the [..[126]]discrete set of sampled lidar and telescope parameters, the maximum of the objective function results in the optimal telescope parameters within the discrete set of sampled lidar and telescope parameters. In this way, we are able to judge the initially chosen telescope parameters.

[117]removed: . The power spectral density (S_k) of the blade effective wind speeds gives more weight to the relevant frequencies where power is concentrated. The final function J is the sum of the three functions J_k

[119]removed: A near-optimal preview time is obtained by delaying the corrected inflow wind speed measurement through an assumption of a preview timerange and evaluation of **??** for each delayed case.

[120]removed: Result

[121]removed: Simulation setup

[122]removed: The reference case we used in this investigation was based on the NREL 5 MW generic wind turbine (Jonkman et al. (2009)) . We used an actuator line model through the coupling between FASTv7 (Fatigue, Aerodynamics, Structures, and Turbulence) aeroelastic simulation code (Jonkman and Buhl (2005)) and PALM (Parallelized Large-Eddy Simulation Model) (Maronga et al. (2015)) as explained by

[123]removed: Bromm et al. (2017)

[124]removed: . The operating conditions corresponded to a resulting hub-height mean wind speed of 13.06 $\mathrm{m\,s^{-1}}$, which is above the rated value of 11.4 $\mathrm{m\,s^{-1}}$. Furthermore, the simulation resulted in a turbulence intensity of 8.5 %, and a wind shear corresponding to a power law description with an exponent of approximate 0.12. The baseline controller of the wind turbine ensured that the generator speed is kept at 1173.7 rpm (Jonkman et al. (2009)), thereby resulting in a mean rotor speed (ω_{r}) of 11.74 rpm and further leading to a 1P frequency of $f_0 = 0.195\,\mathrm{Hz}$.

[125]removed: For an analysis of the induction zone effect, we set the range of the focus distance and telescope position along the blade radius at $F \in [10\,\mathrm{m}, 40\,\mathrm{m}]$, $R \in [20\,\mathrm{m}, and 60\,\mathrm{m}]$, based on a previous investigation (Ungurán et al. (2018)). The range of the other input variables were determined by the results

[126]removed: simulations with laminar inflow and power law wind shear with coefficients of 0.1, 0.2, and 0.3. An approximation of the induction zone effect introduced some uncertainties into the measurement, but they were included in the identified uncertainty weight

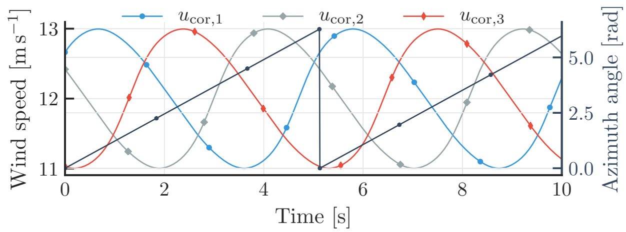

Figure 6. Time series of three generic wind speed measurements at the same amplitude, used for analyzing the impact of the multiblade coordinate transformation. The first, second, and third signals have a phase shift of 30°, 150°, and 270°, respectively. The signals are constructed to include harmonics up to 6P.

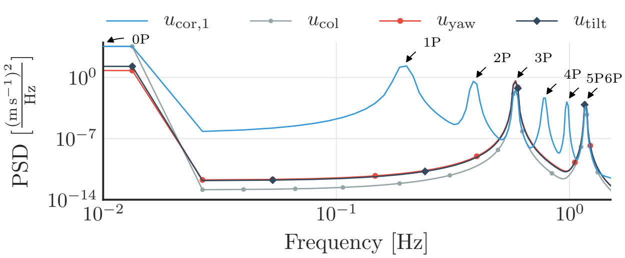

Figure 7. Power spectral [..[128]]densities of the generic signals in the rotating ($u_{\mathrm{cor},1}$) and non-rotating (u_{col}, u_{yaw}, u_{tilt}) frames of reference during the application of the multiblade coordinate transformation.

3 Result

3.1 Multiblade coordinate transformation effect on the blade-mounted lidar measurement

To perform an analysis of the MBC transformation, we [..[127]]create three generic wind speed measurement signals with

$$u_{\mathrm{cor},i} = u_0 + \sum_{j=1}^{6} \frac{1}{j^3} \sin\left(j \left[2\pi f_0 t + (i-1)\frac{2\pi}{3} + \frac{\pi}{6} \right] \right), \tag{21}$$

where u_0, i, f_0, and t are the offset, blade index, 1P frequency, and time, respectively. Here, we considered harmonics of up to 6P ($j = 1 \ldots 6$). Figure 6 shows a sample time series of the generated signals. Figure 7 presents the power spectral [..[129]]densities of the wind speed measurement obtained from the first blade ($u_{\mathrm{cor},1}$) and the collective (u_{col}), yaw (u_{yaw}), and tilt (u_{tilt}) components after the MBC transformation, which [..[130]]is applied on the generic wind speed measurement signals ($u_{\mathrm{cor},1}$, $u_{\mathrm{cor},2}$, $u_{\mathrm{cor},3}$). The figure [..[131]]highlights the MBC transformation keeping only 0P, 3P, and multiples of 3P. As Lu et al.

[127] removed: created
[129] removed: density
[130] removed: was
[131] removed: highlighted

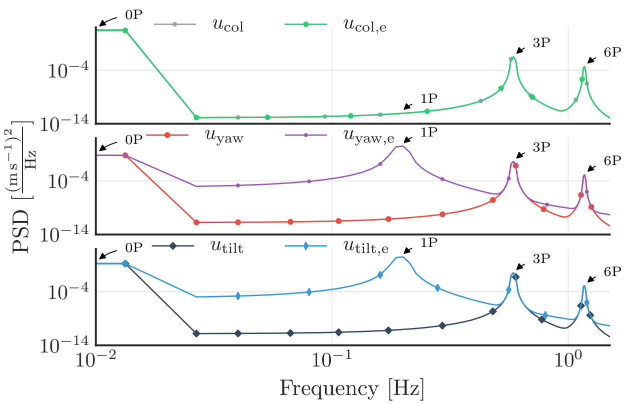

Figure 8. Power spectral [..[136]]densities of collective, yaw, and tilt components of the generic signals with partial DC offset. The expression $\mathrm{u}_{\ldots,\mathrm{e}}$ indicates the case where the DC offset (u_0 in Equation (21)) of one of the signals differs from the other two in the rotating frame of reference.

(2015) [..[132]]describes, the frequency (f) in the non-rotating frame of reference arises from $f \pm f_0$ from the rotating frame of reference, e.g., the 3P in the non-rotating frame of reference arises from the 2P and 4P contributions in the rotating frame of reference.

Several cases may illustrate the transfer of the measurement errors from the rotating to the non-rotating reference frame. First, we should consider the effect of over- or underestimation of the measured wind speed with one of the blade-mounted lidar systems, due to e.g., different radial positions of the telescope along the blade radii or one of the telescopes having a different orientation, which [..[133]]reduces the DC offset (u_0 in Equation (21)) for one of the three generic signals. Next, the signals [..[134]]are transformed into the non-rotating frame of reference, which can be compared to the case where all the DC offsets [..[135]]are maintained for each of the three signals at the same level. As Figure 8 highlights, an undesired peak [..[137]]appears at 1P in the yaw and tilt components in the non-rotating frame of reference, due to the presence of asymmetries in the signals in the rotating frame of reference (Petrović et al. (2015)).

Second, aside from the reduction of the DC offset for one of the signals, a $1°$ of phase shift [..[139]]is added to the 1P harmonics in the rotating frame of reference, which represents the case, for example, where one of the blade-mounted lidar focus distances differs from the other two. Figure 9 reveals that after applying the MBC transformation to the three generic signals, undesired higher harmonic peaks [..[140]]arise in the non-rotating frame of reference. Interestingly, the phase shift that

[132] removed: described
[133] removed: reduced
[134] removed: were
[135] removed: were
[137] removed: appeared
[139] removed: was
[140] removed: rose

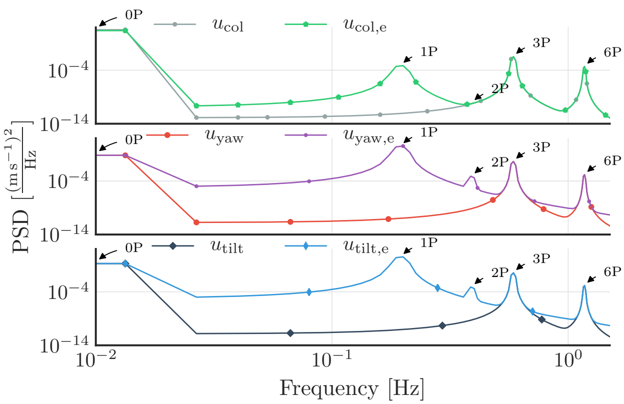

Figure 9. Power spectral [..[138]]densities of collective, yaw, and tilt components of the generic signals with partial DC offset and phase shift. The expression $u_{...,e}$ indicates the case where a different DC offset is set and a 1° of phase shift is added to the 1P harmonics of one of the blade signals in the rotating frame of reference.

[..[141]]is introduced to one of the signals in the rotating frame of reference [..[142]]results in different higher harmonics in the components in the non-rotating frame of reference, e.g., a peak observed at 1P of the collective component and at 2P of the tilt and yaw components.

3.2 [..[143]]Simulation setup

The reference case we used in this investigation is based on the NREL 5 MW generic wind turbine (Jonkman et al. (2009)). We used an actuator line model through the coupling between the FASTv7 aeroelastic simulation code (Jonkman and Buhl (2005)) and PALM (Parallelized Large-Eddy Simulation Model) (Maronga et al. (2015)) as explained by Bromm et al. (2017). The operating conditions correspond to a hub-height mean wind speed of 13.06 $\mathrm{m\,s^{-1}}$, which is above the rated value of 11.4 $\mathrm{m\,s^{-1}}$. Furthermore, the 10-minute simulation results in a turbulence intensity of 8.5 % and a wind shear corresponding to a power law description with an exponent of approximately 0.12. The baseline controller of the wind turbine ensures that the generator speed is kept at 1173.7 rpm (Jonkman et al. (2009)), thereby resulting in a mean rotor speed (ω_{r}) of 11.74 rpm and further leading to a 1P frequency of $f_0 = 0.195$ Hz.

For an analysis of the induction zone effect, we set the range of the focus distance and telescope position along the blade radius at $F \in [10\,\mathrm{m}, 40\,\mathrm{m}]$, $R \in [20\,\mathrm{m}, 60\,\mathrm{m}]$, based on a previous investigation (Ungurán et al. (2018)). The range of the other input variables are determined by the results of simulations with laminar inflow and power law wind shear with coefficients of 0.1, 0.2, and 0.3. An approximation of the induction zone effect introduces some uncertainties into the measurement, but they are included in the identified uncertainty weight.

[141] removed: was
[142] removed: resulted to
[143] removed: Uncertainty weight identification

Table 1. The cases investigated in this study, along with the lidar and telescope parameters for each case. If one or more parameters in the third column are not specified, then the parameters defined in the first case are used. F is the focus length, R is the radial position of the telescope along the blade, and $\Phi_{\ell,i}$ and $\Gamma_{\ell,i}$ are the orientation angles of the telescope.

Case	Uncertainties for:	Parameters
C_1	telescope parameters from [..[144]]literature, assuming: – no induction – no wind evolution – no blade flexibility	$F = 22.2\,\mathrm{m}$ $R = 44\,\mathrm{m}$ $\Phi_{\ell,i} = -3.7°$ $\Gamma_{\ell,i} = 7.0°$
C_2	telescope parameters within prescribed range	$F \in [20.2\,\mathrm{m}, 30\,\mathrm{m}]$ [..[145]]$R \in [42\,\mathrm{m}, 47\,\mathrm{m}]$ [..[146]]$\Phi_{\ell,i} \in [-6.7°, -0.7°]$ [..[147]]$\Gamma_{\ell,i} \in [4°, 10°]$
C_3	different telescope focus length	$F \in [20.2\,\mathrm{m}, 30\,\mathrm{m}]$
C_4	different position of the telescope along the blade radius	[..[148]]$R \in [42\,\mathrm{m}, 47\,\mathrm{m}]$
C_5	different orientation angles of the telescope	$\Phi_{\ell,i} \in [-6.7°, -0.7°]$ $\Gamma_{\ell,i} \in [4°, 10°]$
C_6	telescope orientation misalignment	$\Phi_{\ell,i} = \Phi_{\ell,1} \pm 5°$ $\Gamma_{\ell,i} = \Gamma_{\ell,1} \pm 5°$ with $i = 2, 3$

3.3 Nominal plants and uncertainty weights identification

Ungurán et al. (2019) [..[149]]stress that an elevated peak around the crossover frequency (just below the 1P frequency) of the feedback–feedforward controller sensitivity function leads to increased loads across the wind turbine components. Here, the crossover frequency of the controller [..[150]]is defined where the sensitivity function first crosses [..[151]]-3 dB from below. Uncertainties pose limitations on the achievable performance (Skogestad and Postlethwaite (2005)), e.g., the peak of the sensitivity function may increase due to uncertainties in the system. Therefore, it is important to [..[152]]analyse how the lidar measurement uncertainty is affected by e.g., mounting misalignment of the telescope on the blade, or in cases where the focus distance or position of the telescope along the blade span differs from the optimal parameters, etc. Identifying the lidar measurement uncertainty as a frequency-dependent [..[153]]minimum-phase filter enables the inclusion of such parameters in the control development, allowing an analysis of its impact on the stability and performance of the closed-loop system. A straightforward solution to determine the telescope and lidar parameters, such as focus distance, telescope position along the blade radius, telescope orientation on the blade, etc., is to assume that the blades are rigid, that the rotor speed and pitch angle are constant, and that Taylor's frozen turbulence hypothesis (Taylor (1938)) holds (Ungurán et al. (2018)). We [..[154]]perform large-eddy simulation (LES) in the succeeding sections to examine the usefulness and limitations of these assumptions, and further [..[155]]analyse the uncertainties in the blade-mounted lidar measurement as well as the measurement sensitivity with respect to lidar and telescope parameter changes. The investigated cases are described in Sections 3.3.1 to 3.3.5 [..[156]]and summarized in Table 1. Section 3.3.6 describes how the measurement uncertainties are affected when one or two telescopes are aligned differently than the others. First, we [..[157]]assume that the orientation angle misalignment [..[158]]is unknown. Second, we [..[159]]assume that this orientation angle misalignment can be identified, so that the lidar-based inflow wind speed measurement can be corrected. [..[160]]

For each case, [..[166]]first the transfer functions ($G_{\ell,k}$) from the blade effective wind speeds ($u_{\mathrm{beff,k}}$) to the corrected lidar-based inflow wind speeds ($u_{\mathrm{cor,k}}$) are identified. Next, the [..[167]]nominal disturbance measurement models ($G_{\mathrm{n},k}$) and the uncertainty weights ($w_{\ell,k}$) for each of the inputs are estimated to satisfy [..[168]]Equations (16) and (17). Figure 10

[149] removed: stressed
[150] removed: was
[151] removed: the
[152] removed: analyze
[153] removed: first-order
[154] removed: performed
[155] removed: analyzed
[156] removed: ,
[157] removed: assumed
[158] removed: was
[159] removed: assumed
[160] removed: were
[166] removed: the relative error between the nominal ($G_{\mathrm{n},k}(j\,\omega)$) and the identified ($G_{\ell,k}(j\,\omega)$) systems were first determined
[167] removed: uncertainty weight parameters from Equation (17) were
[168] removed: **??**

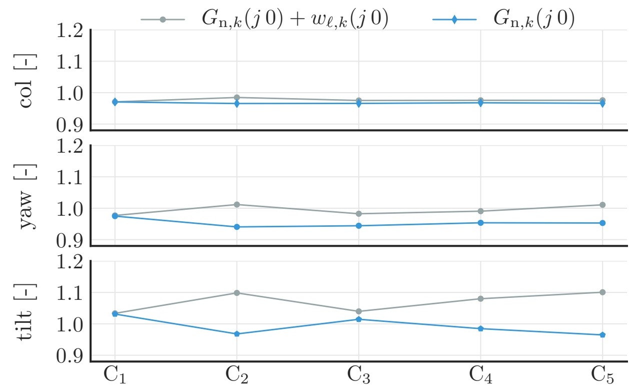

Figure 10. Identified [..[161]]low-frequency (DC) gain upper ($G_{\mathrm{n},k} + w_{\ell,k}$) and [..[162]]lower ($G_{\mathrm{n},k}$) bounds of the [..[163]]transfer functions ($G_{\ell,k}$) from the blade effective wind speeds ($u_{\mathrm{beff,k}}$) to the corrected lidar-based inflow wind speeds ($u_{\mathrm{cor,k}}$), with $k \in \{\mathrm{col, yaw, tilt}\}$; C_1, C_2, C_3, C_4, and C_5 represent the investigated cases ([..[164]]outlined in [..[165]]Table 1).

provides a summary of the [..[169]]identified low-frequency (DC) gain upper ($G_{\mathrm{n},k} + w_{\ell,k}$) and lower ($G_{\mathrm{n},k}$) bounds of the transfer functions ($G_{\ell,k}$) from the blade effective wind speeds ([..[170]]$u_{\mathrm{beff,k}}$) to the corrected lidar-based inflow wind speeds ([..[171]]$u_{\mathrm{cor,k}}$)

We would like to act only below the 1P (0.195 [..[172]]Hz) frequency, therefore, below this frequency, it is desired that the gain of $G_{\mathrm{n},k}$ is 1, and that the measurement uncertainty is small, but still covers the worst case. A higher percentage of measurement uncertainty can be tolerated at frequencies above 1P by designing the feedforward controller accordingly, e.g. a model inversion-based feedforward controller with a low-pass filter with a crossover frequency below 1P. With Figure 10, we show how wide of a low-frequency gain variation of $G_{\ell,k}$ is covered with the identified nominal disturbance measurement models and the additive uncertainty weights.

3.3.1 Telescope parameters for no-induction case ($\mathbf{C_1}$)

The basic concept of the feedforward controller is the use of measured inflow wind speed from blade i to control the blade and trailing edge flap angles at blade $i-1$. Assuming [..[173]]rigid blades, constant rotor speed and pitch angle, and that Taylor's frozen turbulence hypothesis (Taylor (1938)) holds, [..[174]]results a minimum preview time of 1.7 s ($= \frac{2\pi}{3}\frac{30}{\pi\,\omega_\mathrm{r}}$, $\omega_\mathrm{r} = 11.74\,\mathrm{rpm}$)[..[175]], which is the time needed for blade $i-1$ to reach the position of blade i, i.e. 120° azimuth angle change.

[169] removed: estimated parameters. The DC($w_{\mathrm{DC},k}$) and high-frequency gains ($w_{\infty,k}$) of the filter were expressed in percentage, representing the normalized system perturbation away from 1 on that frequency. Thus, 0 % of uncertainty indicates that the identified transfer function (G_ℓ

[170] removed: u_{beff}

[171] removed: u_{cor}) can have a gain of 1 in that frequency. Moreover, 10

[172] removed: % of uncertainty means that the identified transfer function (G_ℓ) can have a gain of either 0.9 or 1.1 in that frequency.

[173] removed: that the blades are rigid

[174] removed: resulted in a

[175] removed: of preview time, or

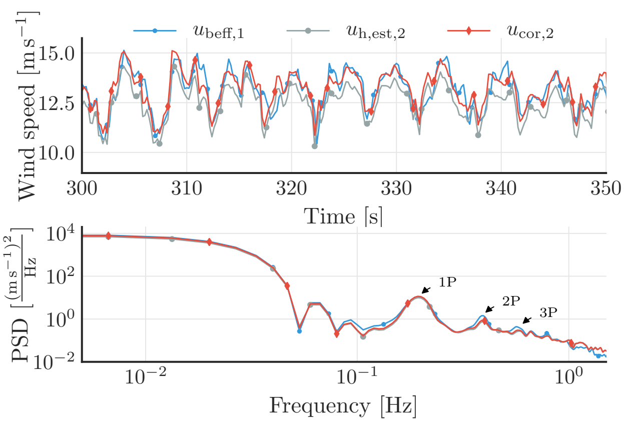

Figure 11. A sample time series of the blade effective wind speed from blade 1 ($u_{\mathrm{beff},1}$) and the estimated ($u_{\mathrm{h,est},2}$) and corrected ($u_{\mathrm{cor},2}$) inflow wind speeds from blade 2 in the rotating frame of reference shown in the upper plot. The power spectral [..[181]]densities (PSD) of the three signals is displayed in the lower plot.

The simulation setup presented in Section 3.2 [..[176]]results in a hub-height mean wind speed of $13.06\,\mathrm{m\,s^{-1}}$. The assumption that the wind evolves according to Taylor's frozen turbulence hypothesis, and with the induction zone effect being negligible, a focus distance of 22.2 m ($= 1.7\,\mathrm{s} \cdot 13.06\,\mathrm{m\,s^{-1}}$) [..[177]]is determined. In accordance with Bossanyi (2013) and Simley et al. (2014a), the inflow at 70 % (≈ 44 m) of the blade radius could be assumed as most representative of the blade effective wind speed; hence, the telescope [..[178]]is located at this radial position. [..[179]]The telescope orientation angles $\Phi_{\ell,i}$ and $\Gamma_{\ell,i}$ [..[180]]are found through aeroelastic-simulation where laminar inflow is considered. The telescope orientation angles are the counter rotation of the blade segment angular orientation so that the lidar beam becomes parallel with the rotor shaft axis (see Figure 2).

Figure 11 (upper plot) shows a sample time series of the blade effective wind speed from blade 1 ($u_{\mathrm{beff},1}$), as well as the estimated ($u_{\mathrm{h,est},2}$) and corrected ($u_{\mathrm{cor},2}$) inflow wind speeds from blade 2. The three signals are in the rotating frame of reference. The lower plot displays the power spectral [..[182]]densities (PSD) of the three signals. The dominant frequencies [..[183]]are clearly visible, as a result of the rotational sampling of the inflow wind speed by the blade-mounted telescope. The

[176]removed: resulted
[177]removed: was
[178]removed: was located in
[179]removed: Specifically, the
[180]removed: were found through the simulation, as
[182]removed: density
[183]removed: were

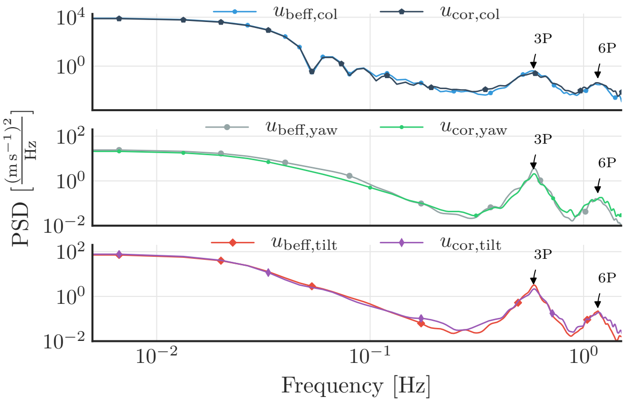

Figure 12. Power spectral [..[187]]densities of the blade effective wind speeds ($u_{\mathrm{beff},k}$) and the corrected inflow wind speeds ($u_{\mathrm{cor},k}$) in the non-rotating frame of reference, with $k \in \{\mathrm{col, yaw, tilt}\}$.

PSD analysis [..[184]]highlights these dominant frequencies as 1P, 2P, and 3P. Moreover, the plot [..[185]]reveals a good match at 1P between $u_{\mathrm{beff,1}}$ and $u_{\mathrm{cor,2}}$, although $u_{\mathrm{cor,2}}$ [..[186]]is slightly underestimated at higher harmonics.

We [..[188]]transform the different blade effective and corrected inflow wind speeds from the rotating to the non-rotating frame of reference via the multiblade coordinate transformation ($T_{\mathrm{mbc}}(\theta)$) [..[189]]as discussed in Section 2.4. Afterward, we [..[190]]evaluate the PSD for the collective, yaw, and tilt components of the signals[..[191]], and the results are displayed in Figure 12. The plot highlights the absence of 1P and 2P components (as observed in the rotating frame of reference, see Figure 11) in the non-rotating frame of reference, in line with Section 2.4. Below 0.1 Hz, a good match between the collective and tilt components [..[192]]are observed, but [..[193]]the yaw component of the corrected inflow wind speed ($u_{\mathrm{cor,yaw}}$) is slightly underestimated. Furthermore, the 3P component of $u_{\mathrm{cor},k}$ (with $k \in \{\mathrm{col, yaw, tilt}\}$) in the non-rotating frame of reference, which is the contribution of 2P and 4P from the rotating frame of reference, [..[194]]is likewise underestimated in all three components.

[184] removed: highlighted
[185] removed: revealed
[186] removed: was
[188] removed: transformed
[189] removed: according to
[190] removed: evaluated
[191] removed: . Figure 12 displays the result
[192] removed: could be
[193] removed: with
[194] removed: was

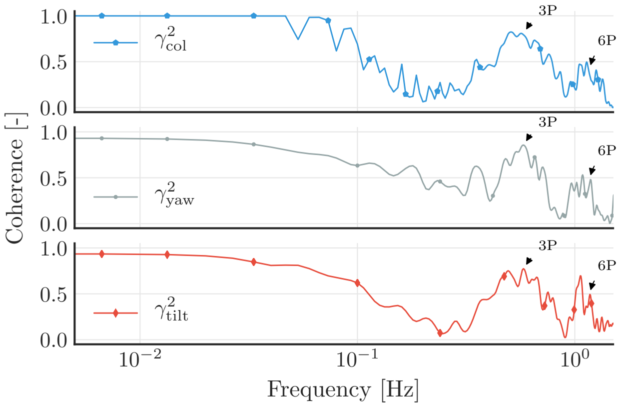

Figure 13. Coherences (γ^2) between the blade effective wind speeds ($u_{\mathrm{beff},k}$) and the corrected inflow wind speeds ($u_{\mathrm{cor},k}$) in the non-rotating frame of reference, with $k \in \{\mathrm{col}, \mathrm{yaw}, \mathrm{tilt}\}$.

Figure 13 reveals a good coherence [..[195]]at the frequencies where the [..[196]]power is concentrated, i.e., below 0.1 Hz, and at 3P and 6P. Additionally, the [..[197]]plots disclose the declining coherence with [..[198]]increasing frequency i.e., higher coherence [..[199]]is achieved at 0P than at 3P; the same could be implied between 3P and 6P. With Figure 11 highlighting the low-power content of the signals between 0P and 3P, and between 3P and 6P, low coherences [..[200]]are similarly seen at the same frequencies in Figure 13.

Furthermore, we [..[208]]determine the disturbance measurement models ($G_{\ell,k}(j\,\omega)$), the nominal disturbance measurement models ($G_{\mathrm{n},k}(j\,\omega)$)[..[209]], and the measurement uncertainty weights ($w_{\ell,k}(j\,\omega)$), shown in Figure 14, which can be incorporated in the feedback–feedforward individual pitch control development and analysis. This case is labelled as C_1 in Figure 10. [..[210]]Figure 14 underline that this case only covers very small gain variations. The figure highlights that the mean value of the corrected inflow wind speed measurement is slightly underpredicted on the collective and yaw components, the low-frequency gain is below 1, and is slightly overpredicted on the tilt component, the low-frequency gain is above 1.

[195] removed: on
[196] removed: powers were
[197] removed: plot discloses
[198] removed: frequency increase
[199] removed: was
[200] removed: were
[208] removed: determined the measurement uncertainty weights for the feedback–feedforward individual pitch control development and analysis. The blue lines in Figure 14 show the relative error between the resulting nominal
[209] removed: and identified ($G_{\ell,k}(j\,\omega)$)plants, in accordance with **??**. The uncertainty weight was approximated with a first-order minimum-phase filter (shown by dashed line), whose parameters from Equation (17) were labeled
[210] removed: Figure 14 shows a low uncertainty on the frequencies where the power of the signals were concentrated. Note that these uncertainties increased at higher harmonics.

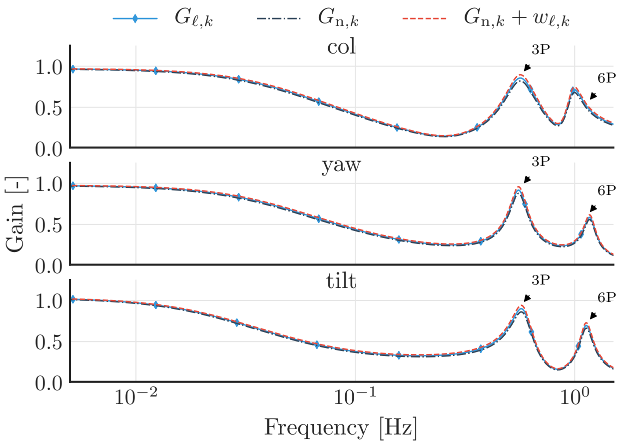

Figure 14. [..[201]]The identified disturbance measurement transfer functions ($G_{\ell,k}(j\,\omega)$). The dashed-dotted lines indicate the estimated nominal [..[202]]disturbance measurement models ($G_{\mathrm{n},k}(j\,\omega)$)[..[203]]. The dashed [..[204]]lines show the sum of the estimated [..[205]]nominal disturbance measurement models and uncertainty [..[206]]weights ([..[207]]$G_{\mathrm{n},k}(j\,\omega) + w_{\ell,k}(j\,\omega)$), where $k \in \{$col, yaw, tilt$\}$.

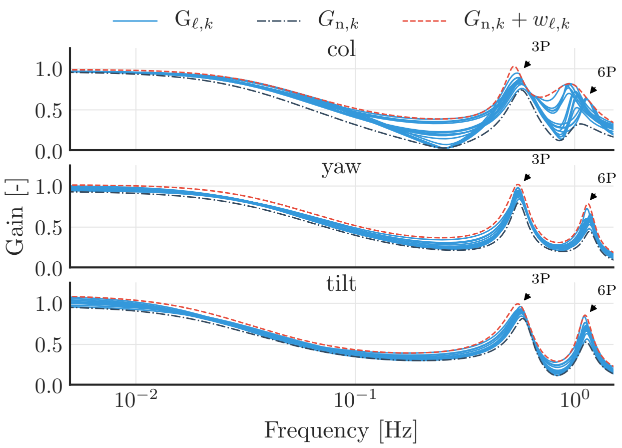

Figure 15. The identified disturbance measurement transfer functions ($G_{\ell,k}(j\,\omega)$) for a discrete set of sampled telescope parameters. The dashed-dotted lines indicate the estimated nominal disturbance measurement models ($G_{\mathrm{n},k}(j\,\omega)$). The dashed lines show the sum of the estimated nominal disturbance measurement models and uncertainty weights ($G_{\mathrm{n},k}(j\,\omega) + w_{\ell,k}(j\,\omega)$), where $k \in$ {col, yaw, tilt}.

3.3.2 Uncertainties around the no-induction telescope parameters ($\mathbf{C_2}$)

In this section, we [..[211]]investigate the impact on the uncertainty weights when the telescope parameters cannot be selected as defined for the no-induction case, but are somewhere close to these values. We carried out simulations involving a discrete set of sampled values for the focus distance, radial position of the telescope along the blade radii, and orientation angles of the telescope. The identified [..[212]]

[..[213]] [..[214]]disturbance measurement transfer functions ($G_{\ell,k}(j\,\omega)$) for the discrete set of sampled values [..[215]]are shown as overlapping blue lines in Figure 15. The plot [..[216]]underscores that the disturbance measurement transfer functions are influenced by the telescope parameters[..[217]]. The low-frequency gain variation is different at each of the three components, which is also seen in Figure 10, where it is labelled as C_2. The highest low-frequency gain variation is observed on the tilt component.

3.3.3 Optimal focus distance and available preview time ($\mathbf{C_3}$)

[..[218]] [..[219]]We determine the preview time in accordance with Section 2.7. We keep the telescope parameters constant as defined in Section 3.3.1, except for the focus distance, which [..[220]]is allowed to vary between 20.2 and 30 m. [..[221]]We

---

[211]removed: investigated

[212]removed: uncertainty weight parameters are labeled as C_2 in Figure 10. The plot shows that the crossover frequencies ($\omega_{0,k}$) for this case (C_2) either remain the same or decreasing slightly with respect to C_1. A significant increase was observed at the low-frequency (DC) uncertainties for the yaw and tilt components, i.e., the low-frequency uncertainties at the yaw and tilt components were changed from the no-induction case values of 8 % and 25 % to 20 % and 43 %, respectively. The high-frequency uncertainties remained nearly the same.

[213]removed: Relative errors between the nominal plants ($G_{\mathrm{n},k}(j\,\omega)$) and those identified ($G_{\ell,k}(j\,\omega)$) for a discrete set of sampled telescope parameters, where $k \in \{\text{col, yaw, tilt}\}$. The relative errors are represented with overlapping grey lines on the plot. The blue line with diamonds is the relative error found for the no-induction case (C_1).

[214]removed: In Figure 15, the overlapping grey lines represent the relative errors

[215]removed: . The blue line with diamonds represents the relative error found for the no-induction case (C_1)

[216]removed: underscored the occurrence of both a better and a worse set of telescope parameters that yield a lower or higher low-frequency uncertainty. For example, after performing a search, we found that the telescope parameters of $F = 20.2$ m, $R = 44.0$ m, $\Phi_{\ell,i} = -5.7°$, and $\Gamma_{\ell,i} = 9°$ would result in the minimum value of $\sum_k \omega_{0,k}$, and

[217]removed: of $F = 28.2$ m, $R = 45.0$ m, $\Phi_{\ell,i} = -1.7°$, whereas $\Gamma_{\ell,i} = 5°$ would result in the maximum value of $\sum_k \omega_{0,k}$, where $k \in \{\text{col, yaw, tilt}\}$

[218]removed: The optimal preview time for a given focus distance. The maximum frequency ($f_{\max}$) in the objective function (J) is set at 0.06 Hz. The green line with the stars is the calculated preview time for the no-induction case. The blue line with the diamonds is a linear fit of the optimal preview time determined for a given focus distance by considering $f_{\max}$ at 0.06 Hz in J.

[219]removed: To determine the optimal preview time , we kept

[220]removed: was

[221]removed: Subsequently, we performed a search at assumed preview times from 1.6 to 2.3 s, with a resolution of 0.2

determine a preview time of 1.9 s for [..[222]]all the [..[223]]focus distances, which is slightly higher than the initially calculated value of 1.7 [..[224]]s in Section 3.3.1.

[..[225]]

[..[226]]This case is denoted as C_3 [..[227]]in Figure 10, and that figure highlights that there is a smaller low-frequency gain variation for this case compared to the previous case (C[..[228]]$_2$).

[..[229]]

3.3.4 Telescope position along the blade span (C_4)

Bossanyi (2013) proposed that a blade-mounted lidar placed at 70 % of the blade radius is most suitable for feedforward control input. We [..[230]]assess in this subsection whether placing the blade-mounted lidar at 70 % (≈ 44 m) of the blade radius would result in the [..[231]]maximum of the objective function in [..[232]]Equation (20). We set f_{max} in [..[233]]Equation (20) as 0.1 Hz, while we maintained a focus distance of 22.2 m. [..[234]]

We find that the telescope placed at a radial position of 46 [..[235]]m leads to the maximum value of the objective function in Equation (20), in other words, the telescope positioned at a radial position of 46 m results in the highest coherence between the blade effective [..[236]]

---

[222]removed: each focus distance. Afterward, we evaluated the objective function from **??** for all combinations of the focus distance and preview time. **??** displays a plot, as a color map, of the result. Accordingly,

[223]removed: green line with the stars indicates the calculated preview time for the no-induction case, as determined by dividing the focus distance (F) with the hub-height mean wind speed ($u_{\text{hh}} = 13.06\,\text{m}\,\text{s}^{-1}$). From Figure 14 in the no-induction case, the uncertainties ($w_{\ell,k}$) at the components were either close or above 100 % around 0.06 Hz; therefore, we considered an f_{max} of 0.06

[224]removed: Hz in **??**. The optimal preview time could be determined for a given focus distance with the minimized objective function (J) in **??**. The blue line with the diamonds shows the resulting optimal preview time for a given focus distance

[225]removed: **??** shows these observations: (1) The values of the objective function increased with measurement distance from the rotor position. (2) The blue line with the diamonds emphasized that a higher preview time was available with respect to the no-induction case (green line with the stars), where the assumptions were (a) the blades are rigid, (b) Taylor's frozen turbulence hypothesis holds, and (c) induction effect is absent. (3) The preview time and focus distance were closely coupled; e.g., a changing focus distance implied a varying preview time.

[226]removed: To estimate the uncertainty weights for this case , we varied the focus distance of the lidar between 20.2 and 30 m with 1 m steps, while the other parameters were kept constant. A summary of the parameters of the uncertainty weights is given in Figure 10,

[227]removed: . By increasing the focus distance, the uncertainties at low-frequencies ($w_{\text{DC},k}$) were increased to almost as much as at C_2 and were almost double those in the no-induction

[228]removed: $_1$).

[229]removed: As such, the results in this subsection highlight the following points:(1) A focus distance close to the rotor is more beneficial, and (2) the inflow wind slows down in front of the rotor due to the induction zone effect, which leads to a higher preview time with respect to the no-induction case.

[230]removed: assessed

[231]removed: minimization

[232]removed: **??**

[233]removed: **??** as 0.06

[234]removed: As such, the corresponding optimal preview time was 1.8

[235]removed: s, which is consistent with that of Section 3.3.3. Selection of the preview time plays an important role, as it affects the phase shift between the two signals in **??**. The corrected inflow wind speed measurement delayed with the preview time to align it with

[236]removed: wind speed.

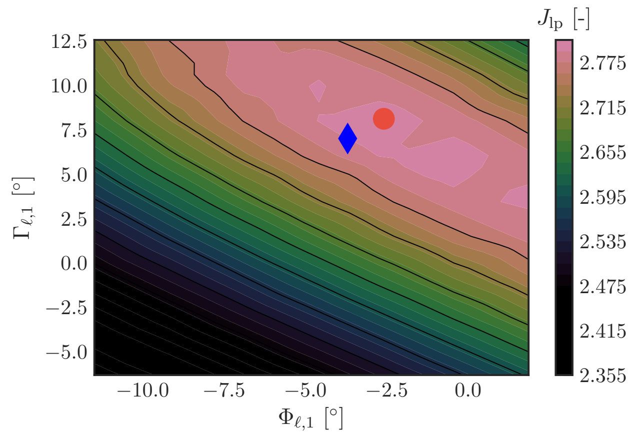

Figure 16. Optimal angular orientation of the telescope. The maximum frequency (f_{max}) in the objective function ([..[247]]J_{lp}) is set at [..[248]]0.1 Hz. The [..[249]]blue diamond marks the initially chosen parameters; and the [..[250]]red dot marks the [..[251]]maximum point [..[252]]of the [..[253]]function from Equation (20).

[..[237]]and the corrected inflow ($u_{cor,k}$) wind speeds. This corresponds to 73 % of the blade span[..[238]]. The found value is quite close to the findings of Bossanyi (2013). [..[239]]Varying the telescope radial position in a fairly small range ([..[240]]42–47 m) [..[241]]results in a higher low-frequency uncertainty on the tilt component than on the collective and yaw components (see C_4 in Figure 10)[..[242]]. In this case, at the yaw and tilt components, the low-frequency gain variation is higher than in C_3, but still smaller than in C_2.

3.3.5 Telescope orientation (C_5)

In this section, we evaluate whether the initially selected telescope orientation angles ($\Phi_{\ell,i}$ and $\Gamma_{\ell,i}$, with $i = 1,2,3$) would result in a [..[243]]maximised objective function in [..[244]]Equation (20). For this purpose, we fixed the telescope parameters as described in Section 3.3.1, with the exception of the orientation angles ($\Phi_{\ell,i}$ and $\Gamma_{\ell,i}$). The two angles [..[245]]are changed around the initially selected values. We [..[246]]simulate the lidar measurements with each new set of parameters. [..[254]]We

[237] removed: Indeed, with the telescope placed at 70

[238] removed: , the objective function in **??** was minimized, confirming

[239] removed: Moreover, varying

[241] removed: yielded a marginal increase (0.004) in the objective function value. A similar effect was observed on the identified uncertainty weight (marked as

[242] removed: , which apparently obtained similar weights parameters as for the no-induction case (C_1), both of which below

[243] removed: minimized

[244] removed: **??**

[245] removed: were

[246] removed: simulated

[254] removed: We used a preview time of 1.8 s for the post-processing, as discussed in Section 3.3.3, which was expected to result in a phase shift of approximately zero between the lidar measurement and the blade effective wind speed at low frequency, below the 1P frequency. We determined

determine the optimal orientation of the telescope in Figure 16 based on the objective function in [..[255]]Equation (20). In the plot, the blue diamond marks the initial telescope orientation based on the no-induction calculation, where $\Phi_{\ell,i} = -3.7°$ and $\Gamma_{\ell,i} = 7.0°$. The [..[256]]red dot indicates the obtained optimal value, where [..[257]]$\Phi_{\ell,i} = -2.6°$ and [..[258]]$\Gamma_{\ell,i} = 8.1°$, which is only marginally different from the no-induction [..[259]]values.

The identified [..[260]]$G_{\ell,k}$ low-frequency (DC) gain upper and lower ($G_{n,k}$) bounds are labelled as C_5 in Figure 10. [..[261]]This case results in a similar low-frequency gains variation as C_2 at the yaw and tilt components, however, it has a smaller gain variation at the collective component than C_2.

3.3.6 Telescope orientation misalignment (C_6)

In this subsection, [..[262]]transfer functions ($G_{\ell,k}$) from the blade effective wind speeds ($u_{\mathrm{beff,k}}$) to the corrected lidar-based inflow wind speeds ($u_{\mathrm{cor,k}}$) are identified for the cases where a single or two of the telescopes have been aligned differently, [..[263]]where their values corresponding to the no-induction case [..[264]]are obtained. Such cases could occur, for example, during telescope installation. Initially, we [..[265]]assume this misalignment as unknown but detectable to allow for the accurate correction of the lidar-based inflow wind speed measurement. To simulate these cases, we fixed the telescope parameters as described in Section 3.3.1, except for the orientation angles of $\Phi_{\ell,i}$ and $\Gamma_{\ell,i}$ of the telescopes mounted on the second and third blades. The angular values [..[266]]are changed around the no-induction values by $\pm 5°$ ($\Phi_{\ell,i} = \Phi_{\ell,1} \pm 5°$ and $\Gamma_{\ell,i} = \Gamma_{\ell,1} \pm 5°$ [..[267]]for $i = 2,3$) as follows. First, the value [..[268]]is changed only for the telescope mounted on the second blade, then for the telescopes mounted on the second and third blades.

We [..[275]]evaluate such setups via simulations. Figure 17 displays the [..[276]]identified transfer functions ($G_{\ell,k}$) from the blade effective wind speeds ($u_{\mathrm{beff,k}}$) to the corrected lidar-based inflow wind speeds ($u_{\mathrm{cor,k}}$). Figure 17a reveals a 1P peak at the collective component and 1P and 2P peaks at the yaw and tilt components. As shown in Section 3.1, adding a phase shift of

[255] removed: **??**

[256] removed: orange star

[257] removed: $\Phi_{\ell,i} = -4.8°$ and $\Gamma_{\ell,i} = 1.45°$. The discrepancy in $\Phi_{\ell,i}$ was quite small, however, with a higher degree of difference between the no-induction value of $\Gamma_{\ell,i}$ and the found optimal value of $\Gamma_{\ell,i}$. To understand such occurrence, we neglected the phase shift (φ_k) in **??**, as marked with a white dot, where

[258] removed: $\Gamma_{\ell,i} = 8.0°$. Thus, the values became considerably closer to the values based on

[259] removed: calculations.

[260] removed: frequency-dependent uncertainty weights parameters were labeled

[261] removed: After the orientation angles were changed by $\pm 3°$ around the no-induction values, the identified uncertainty weight parameters for this case were still close to the values found for the no-induction case

[262] removed: the uncertainty weight parameters were

[263] removed: whereas

[264] removed: were

[265] removed: assumed

[266] removed: were

[267] removed: with

[268] removed: was

[275] removed: evaluated such setups in the

[276] removed: relative errors between the nominal and the identified systems

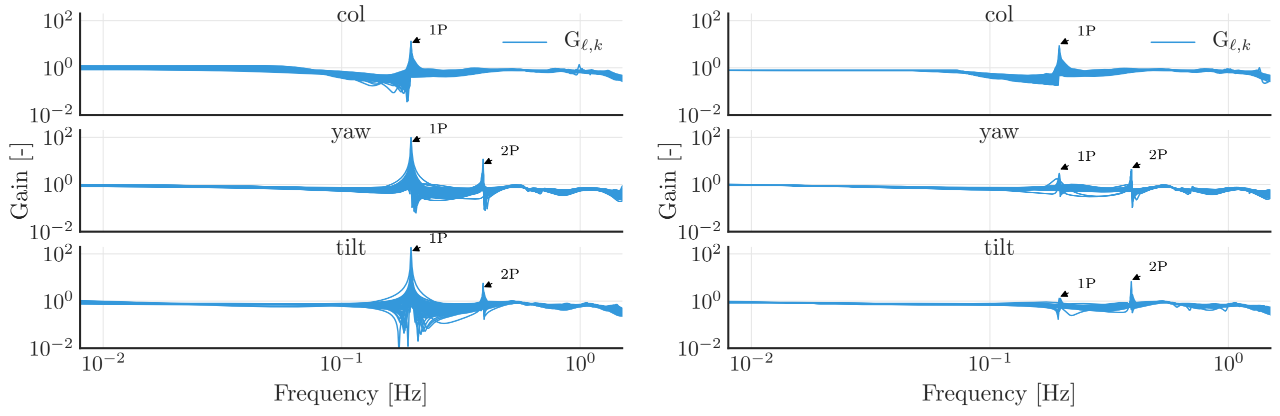

(a) Unknown telescope orientation misalignment.

(b) Known telescope orientation misalignment.

Figure 17. [..[269]]Identified transfer functions ($G_{\ell,k}$) from the [..[270]]blade effective wind speeds ([..[271]]$u_{\mathrm{beff,k}}$) [..[272]]to the corrected lidar-based inflow wind speeds ([..[273]]$u_{\mathrm{cor,k}}$) for the discrete set of sampled telescope parameters with unknown and known telescope orientation misalignment, where $k \in \{\text{col, yaw, tilt}\}$.[..[274]]

1° to the 1P harmonic and reducing the DC offset for one of the signals in the rotating frame of reference [..[277]]results in such undesired higher harmonic peaks at the collective, yaw, and tilt components in the non-rotating frame of reference. Figure 17b underlines that, by assuming that the misalignment angles [..[278]]are identifiable and that the lidar-based inflow wind speed measurement is corrected accordingly, the undesired peak at 1P [..[279]]is reduced by a factor of ten, although existent on all the components. [..[280]]

4 Discussion

We [..[281]]have shown that the determined telescope parameters with assumptions of rigid blades, absence of induction, and Taylor's frozen turbulence hypothesis[..[282]], provide a good trade-off between simplicity and accuracy [..[283]](see C_1 in Figure 10). First, the [..[284]]low-frequency gains of the identified disturbance measurement models ($G_{\ell,k}(j\omega)$) have only small absolute deviations from 1, which are found to be 3 %, 2.5 %, and 3.1 % for collective, yaw, and tilt components, respectively. Second, the found telescope parameters in C_4 and C_5 by means of optimizing a cost function based on the

[277] removed: would result
[278] removed: is
[279] removed: was reduced almost with one decade
[280] removed: Furthermore, the low-frequency uncertainties were reduced significantly on all three components.
[281] removed: showed
[282] removed: hold
[283] removed: . However, we would like to emphasize the presence of uncertainties in all three components, as the result of the wind evolution, the simplicity of the induction zone correction, "cyclops dilemma", and using only a single-point measurement for
[284] removed: estimation of

coherence between the blade effective [..[285]]($u_{\text{beff},k}$) and the corrected inflow ($u_{\text{cor},k}$) wind speeds are close to the initially calculated parameters in C_1. Such a small deviation is expected with respect to the assumptions we made during the calculation of the values for the no-induction case (see Section 3.3.1).

By evaluating the cross-coorelation between the blade effective ($u_{\text{beff},k}$) and the corrected inflow ($u_{\text{cor},k}$) wind speeds for a discrete set of sampled values of the focus distance in Section 3.3.3, we found that the preview time is constant for all the selected focus distances. It is closely coupled to the time needed for blade $i-1$ to reach the position of blade i, i.e. [..[286]]

[..[287]]120° azimuth angle change. For example, by considering laminar inflow with wind shear, no matter what the focus distance is, the [..[288]]delay time between the corrected inflow wind speeds from blade 1 and the blade effective wind speed from blade 3, will always be the same, which is the time needed for blade $i-1$ to reach the position of blade i. If the focus distance has changed, the ϕ in the MBC transformation also has to be changed, furthermore, the control signal should be delayed accordingly. Note that control development must proceed with sufficient attention so as to ensure that the feedforward controller does not result in higher time delay than the available preview time. For example, a feedforward controller with a crossover frequency of [..[289]]0.1 Hz may result in higher time delay compared to that with a crossover frequency of [..[290]]0.2 Hz (Dunne and Pao (2016)). With this, we want to point out that the feedforward controller crossover frequency and the focus distance are coupled. Hence, defining the former typically leads to a minimal selectable focus distance.

As stated above, the lidar and telescope parameters based on the assumptions we made in Section 3.3.1 provide a good trade-off between simplicity and accuracy. They are close to the optimal parameters we found for the discrete set of sampled values of the focus distance, the radial position of the telescope along the blade, and the orientation angles of the telescope [..[291]]in [..[292]]Sections 3.3.3 to 3.3.5. Nevertheless, this is not the case for the preview time; the [..[293]]available preview time is slightly increased from 1.7 s to [..[294]]1.9 s, as we demonstrated in Section 3.3.3. This could be due to the assumptions we made: (a) the blades are rigid, (b) Taylor's frozen turbulence hypothesis holds, and (c) the induction effect is absent during our calculation in Section 3.3.1. Furthermore, the signals were sampled with a sampling time of 0.2 s, which also poses limitations on the resolution of the preview time. Note that LES simulations with lower sampling time are resource

[285] removed: wind speed at assumed zero value of $v_{\mathrm{h},i}$ and $w_{\mathrm{h},i}$ components (see Section 2.1) , etc. Therefore, it is important to consider the uncertainties in the controller development; e.g. , uncertainty at the yaw and tilt components was already approximately 150 % at 0.195 Hz (1P frequency) , which could have affected the performance of the controller

[286] removed: , it can lead to increased values of the sensitivity function, causing load increase on the non-rotating components of the wind turbine, as was asserted by Ungurán et al. (2019).

[287] removed: The results show that the measurement uncertainties increase with distance from the rotor plane. Therefore, a closer measurement of the inflow wind speed to

[288] removed: rotor plane is preferred

[289] removed: 0.06

[290] removed: 0.1

[291] removed: , as shown in

[293] removed: rotor blocking effect increases the

[294] removed: 1.8

and time expensive. The crossover frequency of the feedforward controller affects the time delay. With a higher preview time available, we can select a lower crossover frequency, e.g., where uncertainty is still below 100 %, for the feedforward controller. Note that such uncertainty is defined as the normalized system perturbation away from [..[295]]the nominal system at that frequency; hence, it can be higher than 100 %. This understanding gives us more room during the feedback–feedforward control development. [..[296]]The available preview time [..[297]]could be determined online in field tests [..[298]]and used to delay the feedforward control signal accordingly. This can be done [..[299]]online by, for example, [..[300]]storing ten minutes of blade effective ($u_{\mathrm{beff},k}$) and corrected inflow ($u_{\mathrm{cor},k}$) wind speed measurements, and evaluating the cross-correlation between them.

We found that the blade-mounted lidar placed at the [..[301]]73 % span of the blade radius results in a [..[302]]maximum of the objective function in [..[303]]Equation (20). This finding is [..[304]]close to the value (70 % of the blade radius) found by Bossanyi (2013) for a [..[305]]blade-mounted lidar and Simley et al. (2014a) for the hub-mounted lidar system. [..[306]]

Any unknown orientation angle misalignment for one of the telescopes leads to an unknown contribution of the rotational speed to the lidar-based line-of-sight wind speed measurement. This is the reason [..[307]]why the low-frequency gain can vary between 0.7 and 1.2. Nevertheless, this can be reduced to [..[308]]a low-frequency gain variation between 0.96 and 0.98, by assuming that we are able to detect the angular offset. By detecting the angular offset, we are able to better estimate what is the mean value of the blade effective wind speed, and the resulting $G_{\ell,k}$ low-frequency gain lower bound is 0.96, which is very close to 1. In addition, an undetected misalignment of the telescope orientation angle results in a phase shift of the 1P harmonic and a reduction or increase of the DC offset of the signal in the rotating frame of reference. This subsequently leads to undesired peaks at 1P and 2P frequencies at the collective, yaw, and tilt components in the non-rotating

[295] removed: 1 on

[296] removed: We established a method for estimating the

[297] removed: , which can be extended

[298] removed: for that purpose, as well as

[299] removed: by an online evaluation of **??**

[300] removed: using the last ten minutes estimated blade effective wind speeds and the corrected inflow wind speeds, and then carrying out a similar search we proposed in Section 3.3.3

[301] removed: 70

[302] removed: minimum

[303] removed: **??**

[304] removed: consistent with the conclusion of

[305] removed: blade mounted lidar and is in line with the findings of

[306] removed: The phase shift in the objective function in **??** acts as a fine tuning of the available preview time. We aligned the two signals with the assumption that the measured inflow wind speed hits the wind turbine after 1.8 s, as we found in Section 3.3.3. The signals were sampled with a sampling time of 0.2 s, which limits the fine tuning of the available preview time. Note that LES simulations with lower sampling time are resource and time expensive. When we neglected the phase shift from the objective function, the obtained orientation angles were considerably closer to the orientation angles, based on the no-induction case. Such a small deviation was expected with respect to the assumptions we made during the calculation of the values for the no-induction case (see Section 3.3.1).

[307] removed: for the increase in the uncertainty in the collective component from 3 % to 27 %

[308] removed: 4 %

frame of reference, [..[309]]which we were able to reduce [..[310]]by a factor of ten for both the yaw and tilt components, but we could not completely eliminate these peaks. Thus, the question as to whether robust stability and performance can be ensured with such [..[311]]peaks still remains. To avoid such a peak, the telescopes need to be well aligned with each other, and the blade segment orientation angles and linear velocities should be measured well. We showed in Sections 3.1 and 3.3.6 that an unknown orientation angle misalignment leads to a 1P peak at the yaw and tilt components in the frequency domain. Therefore, the orientation angles of the telescope can be identified by formulating an optimization problem, whose main objective is to minimize the 1P peaks at the yaw and tilt components with orientation angles of the telescopes as the decision variables.

[..[312]]The nominal measurement transfer functions and uncertainty weights identified for the no-induction case can be directly included into robust feedback–feedforward individual pitch and trailing edge flap control development to guarantee robust stability and performance. However, this would be a very optimistic approach, as we considered only one reference wind turbine with a single inflow wind condition and, we need to assess how the measurement uncertainties change for other wind turbines with different wind speeds, turbulence intensities, yaw misalignments, etc. The [..[313]]nominal measurement transfer functions and uncertainty weights found in Section 3.3.2 might cover these cases, and may [..[314]]be helpful in the control development rather than that found in the no-induction case in Section 3.3.1. [..[315]]

[..[316]]

[..[317]]C_2 covers a wide range of telescope parameter variations, hence, if for some reason one or more lidar and telescope parameters cannot be selected as for the no-induction case, but are close to these values, the [..[318]]established transfer functions from C_2 can be used for robust feedback–feedforward control development. [..[319]]In addition, C_2 also covers the situations where the mean blade pitch angle is increased or decreased because of the wind turbine is operating at a different point. The final selection of the nominal measurement transfer functions and uncertainty weights depends on whether the lidar and telescope parameters are varied dynamically with the operating points of the wind turbine and the wind speed, or are kept constant over the entire operating range. Nevertheless, this may further reduce the gains of the feedforward controller[..[320]] (see Ungurán et al. (2019)) with respect to the controller developed by using the nominal

[309] removed: or to nearly 10,000 % of high-frequency uncertainties,

[310] removed: to 1,000 %, but

[311] removed: a high uncertainty still remains, i.e., Ungurán et al. (2019) assumed only 300 % of high-frequency uncertainties on the yaw and tilt components

[312] removed: As

[313] removed: uncertainty weight

[314] removed: serve

[315] removed: Nevertheless, this may further reduce the gains of the feedforward controller (see Ungurán et al. (2019)) with respect to the controller developed by using the uncertainty weight found for the no-induction case, thus limiting the benefits of the lidar system.

[316] removed: We modeled the uncertainty weight as first-order minimum-phase filters. On this regard, if robust performance and stability is not ensured by the use of this weight, then a higher order filter could be studied to observe the relative error over the frequency more closely, e.g., for the tilt component in Figure 14.

[317] removed: The uncertainty weight identified for the no-induction case can be directly included into robust feedback–feedforward individual pitch and trailing edge flap control development to guarantee robust stability and performance. If

[318] removed: uncertainty weight

[319] removed: However, this might lead to a conservative feedforward controller with respect to performance, i.e. , the low-frequency

[320] removed: will be reduced, as highlighted by Ungurán et al. (2019)

measurement transfer functions and uncertainty weights found for the no-induction case, thus limiting the benefits of the lidar system.

The methodology we presented in this paper can be applied in identifying the uncertainty weight for higher harmonics control development, i.e., selecting n_{h} as 2 in Equation (8) can be used to identify the uncertainty weight for the controller developed to mitigate [..[321]]2P dynamic blade loads.

5 Conclusion

Our paper aimed to identify the nominal measurement transfer functions and model the uncertainties of the blade-mounted lidar measurement [..[322]]as a frequency-dependent [..[323]]uncertainty weight for inclusion into the feedback–feedforward individual pitch and trailing edge flap control development[..[324]]

[..[325]], and to analyse the impact of the induction zone effect on the preview time[..[326]].

We found that the preview time [..[327]]with the lidar mounted on the blade is more linked to the time it takes the previous blade to reach the position of the blade from which the measurement took place rather than the focus distance. [..[328]]For a given focus distance, the preview time can be estimated online; hence, the feedforward control signal can be delayed accordingly. While, the selected focus distance should provide sufficient preview time[..[329]], it is desirable that the time delay introduced by the feedforward controller and actuators [..[330]]be eliminated. This sets the lower limit for the selectable focus distance.

Accordingly, we introduced a simple method, based on steady-state data, to calculate the telescope and lidar parameters. Nevertheless, we showed in a large-eddy [..[331]]simulations, that such an approach provides a good trade-off between [..[332]]an efficient determination of the telescope parameters and accurate inflow wind speed measurement. [..[333]]The low-frequency gains of identified disturbance measurement transfer functions had a small absolute deviation from 1, which were due to wind evolution, the "cyclops dilemma", using a single-point measurement to estimate the blade effective wind speed, and the assumptions we made to correct the measurements. The [..[334]]nominal measurement transfer functions and uncertainty

[321] removed: the

[322] removed: uncertainties as

[323] removed: uncertain weights that can be employed in

[324] removed: and analysis.

[325] removed: Typically, induction zone increases

[326] removed: , thus, the latter must be taken into account in the control development and implementation. We presented a method that can estimate

[327] removed: online; hence, the control signal can be delayed accordingly. We found that an inflow wind speed measurement close to the rotor plane is preferable, which emphasizes the influence of the wind evolution, the further the measure takes place from the rotor plane the more the wind develops until it reaches the rotor.

[328] removed: However

[329] removed: so

[330] removed: could

[331] removed: simulation

[332] removed: a fast-forward

[333] removed: Measurement uncertainties were present

[334] removed: uncertainty weight

weights, as we have identified in this paper for several cases, can be directly included in the robust feedback–feedforward individual pitch and trailing edge flap control development to ensure robust stability and performance. However, to prevent the transfer functions (G_ℓ) from the blade effective wind speeds (u_{beff}) to the corrected lidar-based inflow wind speeds (u_{cor}) from having a large high-frequency gain [..[335]]at 1P and 2P in the non-rotating frame of reference, the telescopes must be well aligned with each other and the blade segment orientation angles and linear velocities should be measured well.

Acknowledgements. This work has been partly funded by the Federal Ministry for Economic Affairs and Energy according to a resolution by the German Federal Parliament (projects DFWind 0325936C and SmartBlades2 0324032D). The support of a fellowship from Hanse–Wissenschaftskolleg in Delmenhorst (HWK) is likewise gratefully acknowledged.

[335]removed: of more than 11, which would result in more than 1,000 % high-frequency uncertainties

References

Barlas, T. K., van Wingerden, J.-W., Hulskamp, A. W., van Kuik, G. A. M., and Bersee, H. E. N.: Smart dynamic rotor control using active flaps on a small-scale wind turbine: aeroelastic modeling and comparison with wind tunnel measurements, Wind Energy, 16, 1287–1301, doi:10.1002/we.1560, http://dx.doi.org/10.1002/we.1560, 2013.

Berg, J. C., Resor, B. R., Paquette, J. A., and White, J. R.: SMART wind turbine rotor. Design and field test, Tech. rep., Sandia National Laboratories, 2014.

Bergami, L. and Poulsen, N. K.: A smart rotor configuration with linear quadratic control of adaptive trailing edge flaps for active load alleviation, Wind Energy, 18, 625–641, doi:10.1002/we.1716, 2015.

Bossanyi, E. A.: Individual blade pitch control for load reduction, Wind Energy, 6, 119–128, doi:10.1002/we.76, 2003.

Bossanyi, E. A.: Further load reductions with individual pitch control, Wind Energy, 8, 481–485, doi:10.1002/we.166, 2005.

Bossanyi, E. A.: Un-freezing the turbulence: application to LiDAR-assisted wind turbine control, IET Renewable Power Generation, 7, 321–329, doi:10.1049/iet-rpg.2012.0260, 2013.

Bossanyi, E. A., Kumar, A., and Hugues-Salas, O.: Wind turbine control applications of turbine-mounted LIDAR, in: Journal of Physics: Conference Series, vol. 555, p. 012011, doi:10.1088/1742-6596/555/1/012011, 2014.

Bromm, M., Vollmer, L., and Kühn, M.: Numerical investigation of wind turbine wake development in directionally sheared inflow, Wind Energy, 20, 381–395, doi:10.1002/we.2010, 2017.

Castaignet, D., Barlas, T., Buhl, T., Poulsen, N. K., Wedel-Heinen, J. J., Olesen, N. A., Bak, C., and Kim, T.: Full-scale test of trailing edge flaps on a Vestas V27 wind turbine: active load reduction and system identification, Wind Energy, 17, 549–564, doi:10.1002/we.1589, 2014.

Dunne, F. and Pao, L. Y.: Optimal blade pitch control with realistic preview wind measurements, Wind Energy, 19, 2153–2169, doi:10.1002/we.1973, 2016.

He, K., Qi, L., Zheng, L., and Chen, Y.: Combined pitch and trailing edge flap control for load mitigation of wind turbines, Energies, 11, 2519, doi:10.3390/en11102519, 2018.

Jonkman, J. M. and Buhl, M. L.: FAST user's guide, Tech. rep., National Renewable Energy Laboratory, Golden, Colorado, 2005.

Jonkman, J. M., Butterfield, S., Musial, W., and Scott, G.: Definition of a 5-MW reference wind turbine for offshore system development, Tech. rep., National Renewable Energy Laboratory, Golden, Colorado, 2009.

Kapp, S.: Lidar-based reconstruction of wind fields and application for wind turbine control, Ph.D. thesis, Carl von Ossietzky University of Oldenburg, http://oops.uni-oldenburg.de/3210/1/kaplid17.pdf, 2017.

Laks, J., Simley, E., and Pao, L.: A spectral model for evaluating the effect of wind evolution on wind turbine preview control, in: American Control Conference, pp. 3673–3679, doi:10.1109/ACC.2013.6580400, 2013.

Lu, Q., Bowyer, R., and Jones, B.: Analysis and design of Coleman transform-based individual pitch controllers for wind-turbine load reduction, Wind Energy, 18, 1451–1468, doi:10.1002/we.1769, 2015.

Maronga, B., Gryschka, M., Heinze, R., Hoffmann, F., Kanani-Sühring, F., Keck, M., Ketelsen, K., Letzel, M. O., Sühring, M., and Raasch, S.: The Parallelized Large-Eddy Simulation Model (PALM) version 4.0 for atmospheric and oceanic flows: Model formulation, recent developments, and future perspectives, Geoscientific Model Development, 8, 2515–2551, doi:10.5194/gmd-8-2515-2015, 2015.

Marten, D., Bartholomay, S., Pechlivanoglou, G., Nayeri, C., Paschereit, C. O., Fischer, A., and Lutz, T.: Numerical and experimental investigation of trailing edge flap performance on a model wind turbine, in: 2018 Wind Energy Symposium, AIAA SciTech Forum, American Institute of Aeronautics and Astronautics, doi:10.2514/6.2018-1246, 2018.

MATLAB: version 9.4.0 (R2018a), 2018.

Mikkelsen, T., Siggaard Knudsen, S., Sjöholm, M., Angelou, N., and Tegtmeier, A.: WindScanner.eu - a new remote sensing research infrastructure for on- and offshore wind energy, in: International Conference on Wind Energy: Materials, Engineering, and Policies, 2012.

Navalkar, S., van Wingerden, J.-W., Fleming, P., and van Kuik, G.: Integrating robust lidar-based feedforward with feedback control to enhance speed regulation of floating wind turbines, in: American Control Conference, pp. 3070–3075, doi:10.1109/ACC.2015.7171804, 2015.

Pechlivanoglou, G.: Passive and active flow control solutions for wind turbine blades, Ph.D. thesis, Technical University of Berlin, doi:10.14279/depositonce-3487, 2013.

Petrović, V., Jelavić, M., and Baotić, M.: Advanced control algorithms for reduction of wind turbine structural loads, Renewable Energy, 76, 418–431, doi:10.1016/j.renene.2014.11.051, 2015.

Schlipf, D., Schlipf, D. J., and Kühn, M.: Nonlinear model predictive control of wind turbines using LIDAR, Wind Energy, 16, 1107–1129, doi:10.1002/we.1533, 2013.

Simley, E., Pao, L. Y., Frehlich, R., Jonkman, B., and Kelley, N.: Analysis of light detection and ranging wind speed measurements for wind turbine control, Wind Energy, 17, 413–433, doi:10.1002/we.1584, 2014a.

Simley, E., Pao, L. Y., Gebraad, P., and Churchfield, M.: Investigation of the impact of the upstream induction zone on LiDAR measurement accuracy for wind turbine control applications using Large-Eddy simulation, in: Journal of Physics: Conference Series, vol. 524, p. 12003, 2014b.

Simley, E., Angelou, N., Mikkelsen, T., Sjöholm, M., Mann, J., and Pao, L. Y.: Characterization of wind velocities in the upstream induction zone of a wind turbine using scanning continuous-wave lidars, Journal of Renewable and Sustainable Energy, 8, 013 301, doi:10.1063/1.4940025, 2016.

Skogestad, S. and Postlethwaite, I.: Multivariable feedback control: Analysis and design, 2nd edition, John Wiley & Sons, 2005.

Taylor, G. I.: The spectrum of turbulence, Proceedings of the Royal Society A: Mathematical, Physical and Engineering Sciences, 164, 476–490, doi:10.1098/rspa.1938.0032, 1938.

Ungurán, R. and Kühn, M.: Combined individual pitch and trailing edge flap control for structural load alleviation of wind turbines, in: American Control Conference, pp. 2307–2313, doi:10.1109/ACC.2016.7525262, 2016.

Ungurán, R., Petrović, V., Pao, L. Y., and Kühn, M.: Performance evaluation of a blade-mounted LiDAR with dynamic versus fixed parameters through feedback-feedforward individual pitch and trailing edge flap control, in: Journal of Physics: Conference Series, vol. 1037, p. 032004, doi:10.1088/1742-6596/1037/3/032004, 2018.

Ungurán, R., Boersma, S., Petrović, V., van Wingerden, J.-W., Pao, L. Y., and Kühn, M.: Feedback-feedforward individual pitch control design for wind turbines with uncertain measurements, in: American Control Conference, 2019.

van Engelen, T. G.: Design model and load reduction assessment for multi-rotational mode individual pitch control (higher harmonics control), Tech. Rep. ECN-RX–06-068, Energy Research Centre of the Netherlands, Petten, Netherlands, 2006.

van Wingerden, J.-W., Hulskamp, A., Barlas, T., Houtzager, I., Bersee, H., van Kuik, G., and Verhaegen, M.: Two-degree-of-freedom active vibration control of a prototyped "smart" rotor, IEEE Transactions on Control Systems Technology, 19, 284–296, doi:10.1109/TCST.2010.2051810, 2011.

Zhang, W., Bai, X., Wang, Y., Han, Y., and Hu, Y.: Optimization of sizing parameters and multi-objective control of trailing edge flaps on a smart rotor, Renewable Energy, 129, 75–91, doi:10.1016/j.renene.2018.05.091, 2018.